

NASA/CR-2009-215721



A Mode-Shape-Based Fault Detection Methodology for Cantilever Beams

*Arturo Tejada
NASA Postdoctoral Program
Langley Research Center, Hampton, Virginia*

May 2009

NASA STI Program . . . in Profile

Since its founding, NASA has been dedicated to the advancement of aeronautics and space science. The NASA scientific and technical information (STI) program plays a key part in helping NASA maintain this important role.

The NASA STI program operates under the auspices of the Agency Chief Information Officer. It collects, organizes, provides for archiving, and disseminates NASA's STI. The NASA STI program provides access to the NASA Aeronautics and Space Database and its public interface, the NASA Technical Report Server, thus providing one of the largest collections of aeronautical and space science STI in the world. Results are published in both non-NASA channels and by NASA in the NASA STI Report Series, which includes the following report types:

- **TECHNICAL PUBLICATION.** Reports of completed research or a major significant phase of research that present the results of NASA programs and include extensive data or theoretical analysis. Includes compilations of significant scientific and technical data and information deemed to be of continuing reference value. NASA counterpart of peer-reviewed formal professional papers, but having less stringent limitations on manuscript length and extent of graphic presentations.
- **TECHNICAL MEMORANDUM.** Scientific and technical findings that are preliminary or of specialized interest, e.g., quick release reports, working papers, and bibliographies that contain minimal annotation. Does not contain extensive analysis.
- **CONTRACTOR REPORT.** Scientific and technical findings by NASA-sponsored contractors and grantees.

- **CONFERENCE PUBLICATION.** Collected papers from scientific and technical conferences, symposia, seminars, or other meetings sponsored or co-sponsored by NASA.
- **SPECIAL PUBLICATION.** Scientific, technical, or historical information from NASA programs, projects, and missions, often concerned with subjects having substantial public interest.
- **TECHNICAL TRANSLATION.** English-language translations of foreign scientific and technical material pertinent to NASA's mission.

Specialized services also include creating custom thesauri, building customized databases, and organizing and publishing research results.

For more information about the NASA STI program, see the following:

- Access the NASA STI program home page at <http://www.sti.nasa.gov>
- E-mail your question via the Internet to help@sti.nasa.gov
- Fax your question to the NASA STI Help Desk at 443-757-5803
- Phone the NASA STI Help Desk at 443-757-5802
- Write to:
NASA STI Help Desk
NASA Center for AeroSpace Information
7115 Standard Drive
Hanover, MD 21076-1320

NASA/CR-2009-215721



A Mode-Shape-Based Fault Detection Methodology for Cantilever Beams

*Arturo Tejada
NASA Postdoctoral Program
Langley Research Center, Hampton, Virginia*

National Aeronautics and
Space Administration

Langley Research Center
Hampton, Virginia 23681-2199

Prepared for Langley Research Center
under Contract NNH06CC03B

May 2009

Acknowledgments

This research was supported by an appointment to the NASA Postdoctoral Program at Langley Research Center, administered by Oak Ridge Associated Universities through a contract with NASA.

The use of trademarks or names of manufacturers in this report is for accurate reporting and does not constitute an official endorsement, either expressed or implied, of such products or manufacturers by the National Aeronautics and Space Administration.

Available from:

NASA Center for AeroSpace Information
7115 Standard Drive
Hanover, MD 21076-1320
443-757-5802

Abstract

An important goal of NASA's Internal Vehicle Health Management program (IVHM) is to develop and verify methods and technologies for fault detection in critical airframe structures. A particularly promising new technology under development at NASA Langley Research Center is distributed Bragg fiber optic strain sensors. These sensors can be embedded in, for instance, aircraft wings to continuously monitor surface strain during flight. Strain information can then be used in conjunction with well-known vibrational techniques to detect faults due to changes in the wing's physical parameters or to the presence of incipient cracks.

To verify the benefits of this technology, the Formal Methods Group at NASA LaRC has proposed the use of formal verification tools such as PVS. The verification process, however, requires knowledge of the physics and mathematics of the vibrational techniques and a clear understanding of the particular fault detection methodology.

This report presents a succinct review of the physical principles behind the modeling of vibrating structures such as cantilever beams (the natural model of a wing). It also reviews two different classes of fault detection techniques and proposes a particular detection method for cracks in wings, which is amenable to formal verification. A prototype implementation of these methods using Matlab [®] scripts is also described and is related to the fundamental theoretical concepts.

Contents

1	Introduction	4
2	Basic Concepts from Mechanics of Materials	5
2.1	Normal Stress and Strain	5
2.2	Shear Stress, Shear Strain, and Bending Moment	6
2.3	Beams under Deflection	8
2.4	Summary	10
3	The Equation of Motion Associated with a Vibrating Cantilever	10
3.1	The Method of Dynamic Equilibrium	11
3.1.1	Solution of the Frictionless EOM	13
3.1.2	Solution of the EOM including Friction	15
3.1.3	Simulation of the Equation of Motion	18
3.2	The Hu-Washizu-Barr Variational Principle	19
3.2.1	Derivation of the Frictionless Homogeneous EOM using Variational Methods	20
3.2.2	Derivation of the EOM Associated with a Cracked Cantilever Using Variational Methods	23
3.2.3	Solution of the EOM Associated with a Cracked Cantilever	24
4	Fault Detection Methods for Cantilever Beams	27
4.1	Frequency-Based Detection Methods	27
4.2	Mode-Shaped-Based Detection Methods	28
4.3	A Mode-Shaped-Based Fault Detection Methodology	30
5	Conclusions and Future Research Directions	31
A	Software Components	35

List of Figures

1	Basic structural elements. Left: A cylindrical rod under normal tension. Right: Cantilever beam under transversal load.	5
2	Structural element subject to shear stress and strain.	6
3	Beam detail used to derive the relationship between loads, shear forces, and bending moments.	7
4	Deformation of a beam in pure bending: (left) side view of beam and (right) deformed beam.	9
5	Top left: Normal stresses in a linear elastic bar under pure bending. Bottom left: Cross section view. Right: Deflection curve in a cantilever beam.	10
6	Geometry of the prismatic cantilever beam under consideration. The table lists the cantilever's main parameters.	11
7	Free body diagram (left) and detail (right) of an infinitesimal cantilever segment.	12
8	The first five (vibration) mode shape functions. The horizontal axis is normalized, so the shapes are independent of the beam's length.	14
9	Plot of C_n/B_nL as a function of n	17
10	Cantilever representation appropriate for simulation.	18
11	Output of the programs DATA4SIM_CANTILEVER.m and SHAPE_CANTILEVER.mdl. The cantilever is loaded with $\ell(t) = \sin(13.4854t)$, which excites (only) the first natural oscillation mode.	19
12	Mode shape functions of an undamaged cantilever (dotted blue line) and a single-edge-cracked cantilever (solid red line). The crack position is $x_c = 0.5L$ and its depth is $a = 0.1D$. The plots were generated using the Ritz-Galerkin method with ten basis ($N=10$).	26
13	Setup for a frequency-based fault detection test.	27
14	Comparison of fault detector responses using phase measurements: Undamaged cantilever (solid blue) and damaged cantilever (dashed red).	28
15	Experimental setup for the proposed mode-shape-based fault detection methodology.	30
16	Proposed software verification testbed.	31

1 Introduction

An important goal of NASA's Internal Vehicle Health Management program (IVHM) is to develop new methods and technologies for fault detection in critical airframe structures [1]. This challenge requires not only to develop new hardware and software components, but also to verify their implementations and their capability to detect faults. For example, if a new sensor technology claims to detect 90% of incipient cracks in a wing's surface, not only the sensor implementation must be verified but the claim that it uncovers 90% of the cracks must also be verified.

NASA Langley Research Center is answering this challenge by developing a new promising technology for the detection of incipient cracks in wing surfaces, which uses distributed Bragg fiber optic strain sensors. Moreover, it plans to leverage the expertise at NASA LaRC's Formal Methods Group to develop a sound verification method using formal verification tools. The use of these tools, however, requires a clear understanding of the physics and mathematics behind the fault detection technology.

This report, which is the result of a four-month preliminary study on this subject, aims to provide this understanding. Its goals are to provide the fundamental concepts behind the new detection technology and to propose a detection algorithm for the detection of cracks that is amenable to formal verification.

Detection methods based on strain sensors make use of data collected during the operation of the structure under analysis. In the particular case of an airplane wing, the strain data is collected while the wing vibrates as a result of an external stimulus, usually an external sinusoidal load. The data is then processed to extract parameters that characterize a mathematical model of the wing's response to the load, which are ultimately compared to the ideal parameters of the wing.

The simplest mathematical model of a vibrating wing is a cantilever beam. This model is readily available in the literature for undamaged beams. As will be shown in the sequel, the model of a vibrating cantilever is a fourth-order partial differential equation. The derivation of this equation of motion (EOM) using dynamical equilibrium concepts has been included in the report to introduce the basic concepts needed for fault detection (such as mode shape functions) and to introduce a new system-theoretical view of the cantilever which is amenable for dynamical simulation using Matlab [®] and Simulink [®].

The report also includes a second method to derive the EOM: the Hu-Washizu-Barr variational principle. This more advanced method yields not only the EOM associated with an undamaged cantilever beam, but also the EOM associated with a cracked beam. The latter equation can be solved using the Ritz-Galerkin method, which is based on the solution of the EOM of the undamaged cantilever. The solution of both equations is discussed in detail in Section 3.

Several methods are available to extract the model's parameters from experimental data and to detect faults (if present). The detection methods can be broadly classified into frequency-based methods and mode-shape-based methods. Both types of methods are reviewed succinctly in Section 4, which also presents a detection algorithm that is amenable to formal verification. It is important to remark that most of the analysis is based on the theory of statics and dynamics of structures developed in [2-4]. Additionally, all the numerical examples are based on data provided in [5].

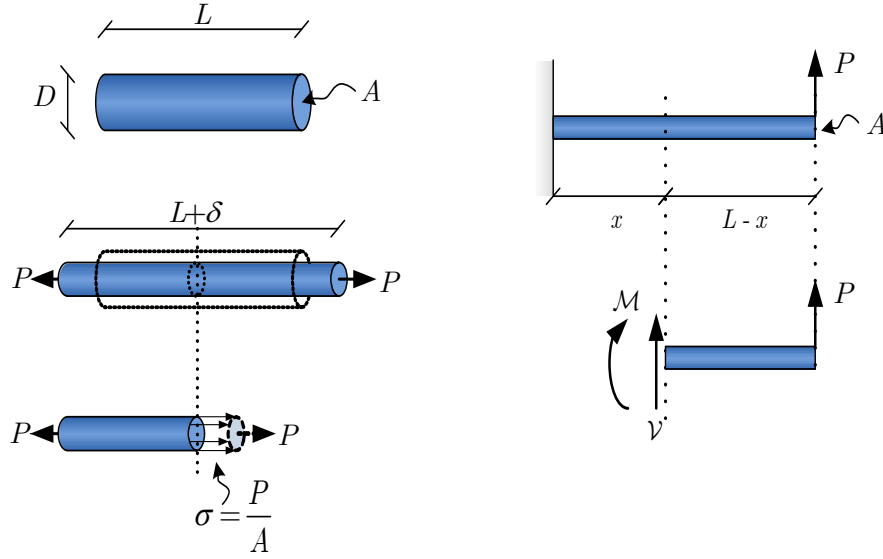


Figure 1. Basic structural elements. Left: A cylindrical rod under normal tension. Right: Cantilever beam under transversal load.

The rest of the report is organized as follows: The basic concepts of mechanics of materials are summarized in Section 2. This is followed by the derivation of the EOM for both undamaged and cracked cantilever beams in Section 3. This section also includes a method to simulate the EOM using Matlab [®] and Simulink [®]. Section 4 reviews the standard vibration-based crack detection methods for cantilever beams, and Section 5 provides our conclusions and directions for future research. Finally, the Appendix provides a list of the Matlab [®] scripts that have been developed to illustrate the concepts described in the report.

2 Basic Concepts from Mechanics of Materials

This section summarizes the basic concepts from mechanics of materials presented in [3]. The goal is to provide common background and terminology to support the analysis of the vibrating cantilever presented in the next section. It is important to remark that all the figures in this section were also taken from [3].

2.1 Normal Stress and Strain

Consider the prismatic bar shown in Figure 1 (left). “A **prismatic bar** is a straight structural member having the same cross section throughout its length” [3]. When it is subject to an axial force P normal to its cross section, its length increases from L to $L + \delta$. For an isotropic bar, the elongation per unit length or **normal strain**, ϵ , is computed as

$$\epsilon = \frac{\delta}{L}.$$

Moreover, P can be assumed to be distributed evenly throughout any of the bar’s cross sections (Figure 1 (left)). Thus, the load per unit area or **normal stress**, σ , is given by

$$\sigma = \frac{P}{A}.$$

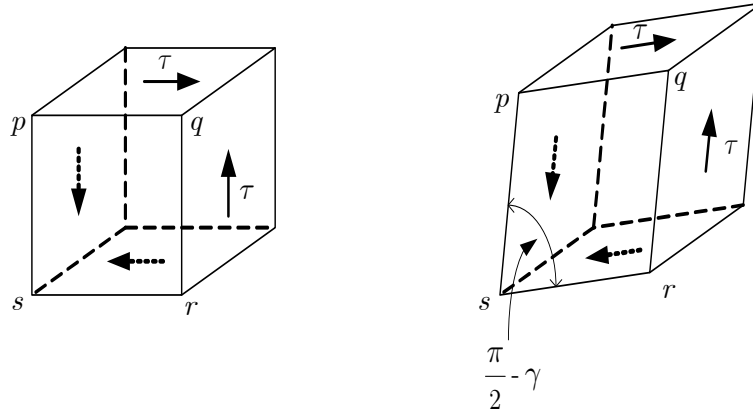


Figure 2. Structural element subject to shear stress and strain.

As a rule, this expression is valid only for cross sections that are located at a distance from the force's point of application that is greater than the bar's biggest lateral dimension (D in this case), provided that P acts through the cross sections' centroid. The normal strain is, by convention, positive when the bar is under tension and negative when it is under compression.

“Many structural materials such as metals, woods, plastics, and ceramics, behave both elastically and linearly when first loaded” [3]. For these kinds of materials, the relationship between normal stress and normal strain under an axial force is given by Hooke's Law

$$\sigma = E\epsilon,$$

where E is known as the **modulus of elasticity or Young's Modulus**. Note that the axial elongation (or compression) is accompanied by a contraction (or elongation) normal to the direction of the force P . If the material is linearly elastic, the **lateral strain** ϵ^* is proportional to the normal strain ϵ . That is,

$$\epsilon^* = -\nu\epsilon,$$

where ν is called the **Poisson's ratio** and the minus sign indicates that the lateral and normal strains have opposite signs (ν is always positive).

Finally, note that in general ϵ , ϵ^* , and σ may vary as functions of the position along the bar's main axis.

2.2 Shear Stress, Shear Strain, and Bending Moment

Structural elements may also be subject to forces which are tangential to their surfaces. As an illustration consider the cantilever bar shown in Figure 1 (right). The applied transversal

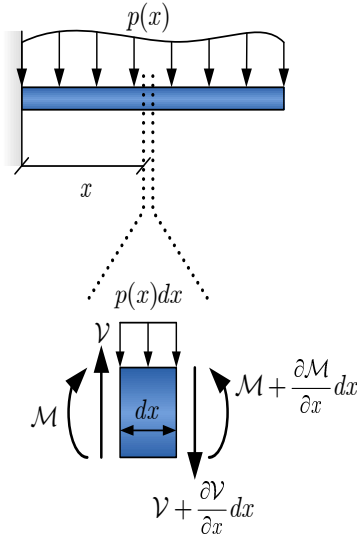


Figure 3. Beam detail used to derive the relationship between loads, shear forces, and bending moments.

load P creates internal forces and moments that keep the cantilever under static equilibrium, as shown in the free body diagram in Figure 1 (bottom right). In this diagram, \mathcal{V} and \mathcal{M} are called, respectively, the **shear force** and the **bending moment**. They are shown in the directions that are assumed, by convention, to be positive. \mathcal{V} tends to ‘cut’ the cantilever beam (hence its name). The distribution of \mathcal{V} over the cross section area is called the **average shear stress** and is given by

$$\tau = \frac{\mathcal{V}}{A}.$$

A body subject to shear stress is deformed as shown in Figure 2. The measure of this deformation is given by the **shear strain** angle γ . For linear elastic materials, τ and γ are related by **Hooke’s law in shear**

$$\tau = G\gamma,$$

where G is the **shear modulus of elasticity** (also known as modulus of rigidity). The parameters E , ν , and G are related by the following expression

$$G = \frac{E}{2(1 + \nu)}. \quad (1)$$

In general, the shear stress, the shear force, and the bending moment vary with position. For the cantilever in Figure 1 (top right), it is clear that $\mathcal{V}(x) = -P$ and $\mathcal{M}(x) = (L - x)P$ for every position x . Observe in this example that $\frac{\partial \mathcal{M}(x)}{\partial x} = -P = \mathcal{V}(x)$. This relationship is also true in the presence of distributed loads. To see this, consider the cantilever in Figure 3 which is subject to a distributed load $p(x)$. On each small beam element, $p(x)$ induces the internal shear forces and bending moments that are shown in the free body diagram in Figure 3. The equilibrium of moments around the lower left corner of the cantilever requires

that

$$\mathcal{M}(x) + (p(x)dx)dx - (\mathcal{M}(x) + \frac{\partial \mathcal{M}(x)}{\partial x}dx) + (\mathcal{V}(x) + \frac{\partial \mathcal{V}(x)}{\partial x}dx)dx = 0.$$

Since $(dx)^2 \approx 0$ this expression yields

$$\mathcal{V}(x) = \frac{\partial \mathcal{M}(x)}{\partial x}. \quad (2)$$

Finally, observe that the equilibrium of forces in the vertical axis requires that

$$p(x)dx + (\mathcal{V}(x) + \frac{\partial \mathcal{V}(x)}{\partial x}dx) - \mathcal{V}(x) = 0,$$

which in turn yields

$$\frac{\partial \mathcal{V}(x)}{\partial x} = -p(x). \quad (3)$$

As will be shown in the next section, these equations (2) and (3) are fundamental to determine the shapes a cantilever takes when subject to loads. The next subsection states the relationship between bending moments and strains in a deflected beam

2.3 Beams under Deflection

A beam is said to be under **pure bending** if it is subject to a constant bending moment throughout its length. As equation (2) shows, this implies that $\mathcal{V}(x) = 0$ for all x . Although the latter does not always hold true in practice, assuming pure bending usually yields good numerical approximations compared to more accurate assumptions [3].

Thus, consider the beam under pure bending shown in Figure 4 (left) and let L denote its length before bending. Under the action of the bending moment \mathcal{M} , the beam deflects as shown in Figure 4 (right). Note that the beam's upper portion is under compression. Thus, in that portion, the length of a surface parallel to the plane $x - y$ decreases (for instance $|AB| < L$ on bending). The opposite happens on the bottom of the beam since it is under tension. Consequently, there exists a **neutral surface** whose length does not change. The intersection of this surface with the plane $x - z$ is called the **neutral axis** (the $s - s$ line in Figure 4) and can be shown to go through the centroid of the beam's cross sections [3].

Consider next the planes containing the cross sections mn and pq and observe that $|mp| = |nq| = |ef| = dx$. When the beam is deflected, these planes intersect at O^* forming a small angle $d\theta$. If $1/\kappa$ denotes the radius of curvature of the neutral axis (κ is called the **curvature**), then $d\theta = \kappa dx$. Moreover, after bending, $|ef| = (1/\kappa - z)d\theta = (1 - \kappa z)dx$. That is, its original length has been reduced by $-(\kappa z)dx$. Consequently, if the beam is linearly elastic, the strain and stress at the ef segment are given by

$$\epsilon_x(z) = -\kappa z \quad \text{and} \quad \sigma_x(z) = -E\kappa z, \quad (4)$$

where the x subscripts indicate that the strain and the stress act in the x -axis direction. This is the so-called **strain-curvature relation** and leads to the moment-curvature equation. The latter can be obtained by realizing that the bending moment and the moment generated by the normal stress must cancel each other in order to attain equilibrium. Thus, using the free body diagram in Figure 5 (left) it is possible to show that

$$\mathcal{M} = - \int_A \sigma_x z dA = \int_A \kappa E z^2 dA = \kappa E \int_A z^2 dA.$$

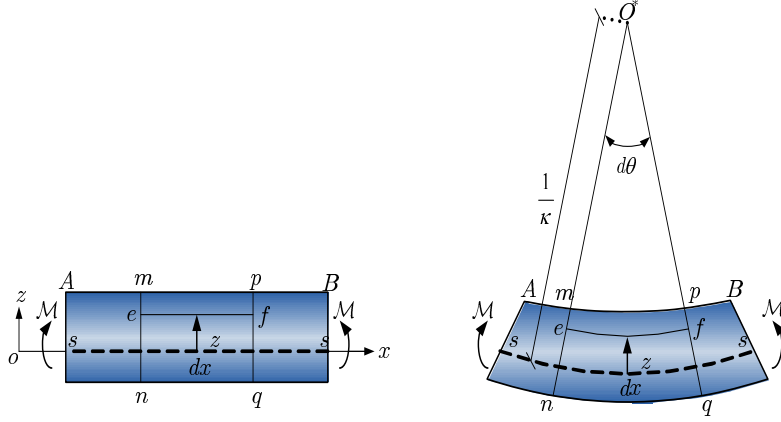


Figure 4. Deformation of a beam in pure bending: (left) side view of beam and (right) deformed beam.

Letting $I \triangleq \int_A z^2 dA$ yields the **moment-curvature relation**

$$\mathcal{M} = EI\kappa. \quad (5)$$

Note that in general the strain, the stress, the curvature and the bending moment may vary with the position along the x -axis. This dependency will be made explicit in the sequel, when needed.

Finally, the differential equation that describes the deflection curve of a cantilever beam can be derived with the setup shown in Figure 5 (right). Let $w(x)$ denote the deflection of its neutral axis in the z -direction at position x . Consider also a small beam segment at position x of length dx . Note that that the center of curvature, O^* , and the radius of curvature, $1/\kappa$, may both be functions of x . Moreover, observe from this figure that

$$\kappa(x) = \frac{d\theta(x)}{ds} \quad \text{and} \quad \frac{dw(x)}{dx} = \tan(\theta(x)).$$

Thus, under *small* deflections one gets that $\theta \approx \tan(\theta(x))$ and $\cos(\theta(x)) \approx 1$, so $dx = \cos(\theta(x))ds \approx ds$ and

$$\kappa(x) \approx \frac{d\theta(x)}{dx} \approx \frac{d}{dx} \left(\frac{dw(x)}{dx} \right). \quad (6)$$

This and (5) yield the **differential equation of the deflection curve**

$$\mathcal{M}(x) = EI \frac{d^2 w(x)}{dx^2}. \quad (7)$$

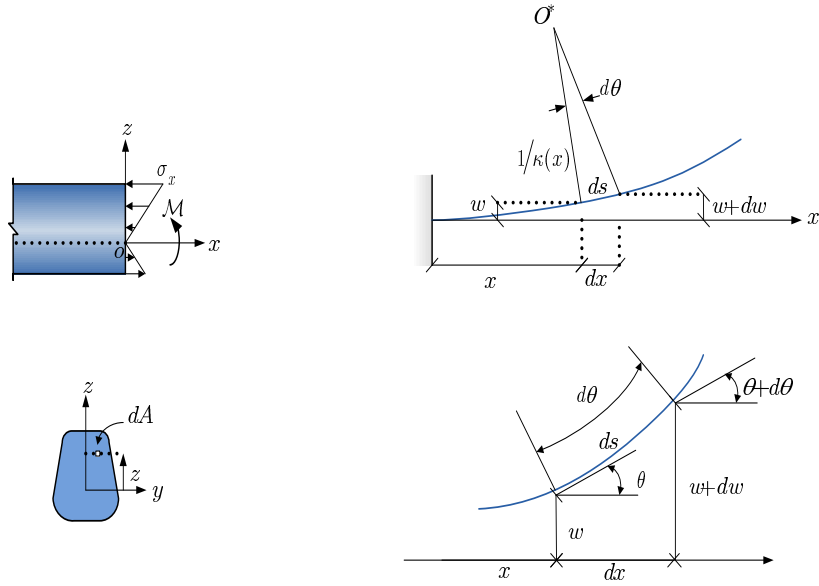


Figure 5. Top left: Normal stresses in a linear elastic bar under pure bending. Bottom left: Cross section view. Right: Deflection curve in a cantilever beam.

2.4 Summary

This section summarized the basic concepts on mechanics of materials as presented in [3]. It was shown that the normal stress, bending moment, curvature, and deflection on a beam can be related by equations (4)-(7) under the following assumptions:

- A1 The beam is prismatic, homogeneous, isotropic, and linearly elastic. It has constant density, ρ , Young's coefficient, E , and viscous damping coefficient, C_s (see below).
- A2 The beam is subject to pure deflection only. No additional shear or axial forces are considered.
- A3 Under bending, cross sections remain planar (Navier's Hypothesis).
- A4 The beam is subject to small deflections only. As a rule of thumb, this means that the largest deflection should be smaller than $1/20$ of the beam's length.
- A5 The bending moment is constant or varies slowly (this improves the approximation of (5)).

The next section builds on these concepts and derives the equation of motion of a vibrating cantilever beam.

3 The Equation of Motion Associated with a Vibrating Cantilever

The focus of this section is to derive the equation of motion (EOM) of a vibrating cantilever beam. The beam geometry and frame of reference is shown in Figure 6. The cantilever is subject to a time-varying distributed load, $p(x, t)$, which acts in the $x - z$ plane. In addition,

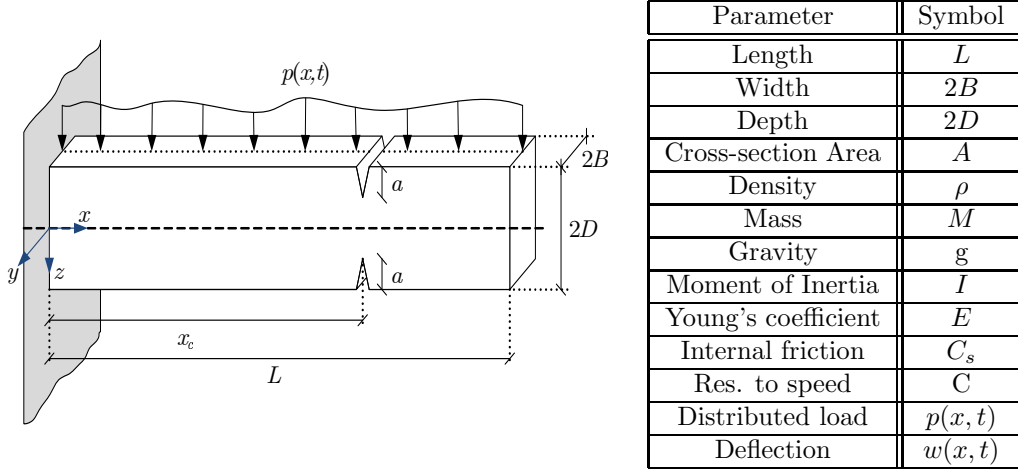


Figure 6. Geometry of the prismatic cantilever beam under consideration. The table lists the cantilever's main parameters.

the cantilever is subject to internal and external friction forces (not shown in the Figure). The internal friction force represents the resistance to strain velocity and the external friction opposes the transverse velocity. These loads induce vibrations in the z -axis that, as will be shown shortly, are governed by a fourth-order partial differential equation. The specific structure and parameters of the EOM depend on the cantilever geometry (e.g., cross section shape) and physical parameters, and on the presence or absence of cracks (Figure 6 shows a pair of symmetric cracks located a distance x_c from the fixed end). The EOM can be derived by at least two different methods: dynamic equilibrium (Newton's second law) and the Hu-Washizu-Barr variational principle (calculus of variations).

The latter makes use of more advanced concepts and is convenient only to analyze beams with cracks. Consequently it will be presented after the following explanation of the dynamic equilibrium method, which builds on the concepts summarized on Section 2. The following additional assumptions are required.

- A6 The beam is Euler-Bernoulli. That is, transverse deflections do not result in axial torsion or rotational shear forces.
- A7 The internal friction coefficient, C_s , is assumed to be proportional to the beam's Young's modulus, i.e., $C_s = a_1 E$.
- A8 The external friction coefficient, C , is proportional to the beam's mass per unit length, i.e., $C = a_0 A \rho$.

Although the cantilever shown in Figure 6 is prismatic, the derivation of the EOM that follows can be applied to non-prismatic beams, that is, to beams with possibly varying cross sectional areas, $A(x)$, masses, $m(x)$, and inertias, $I(x)$.

3.1 The Method of Dynamic Equilibrium

This method is based on Newton's second law: If inertial forces are taken into account, then each section of the cantilever must remain in static equilibrium at every time instant. Thus, consider the free-body diagram of an infinitesimal cantilever segment of length dx , which is shown in Figure 7 (left). Note that all forces, moments, stresses, and strains are functions

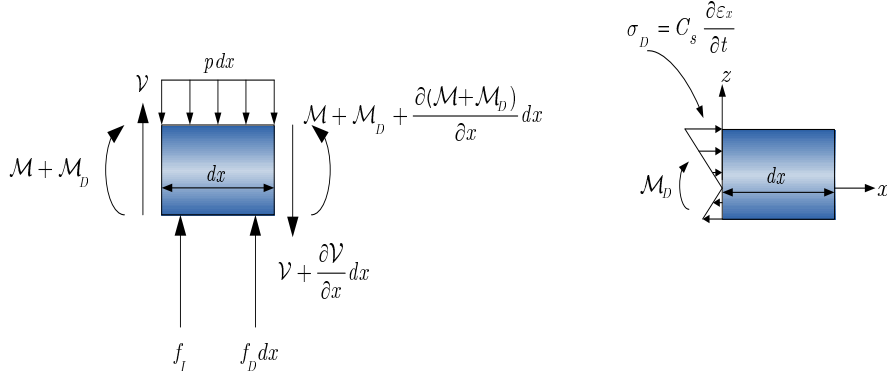


Figure 7. Free body diagram (left) and detail (right) of an infinitesimal cantilever segment.

of time and of the segment's position, x .

In this figure, $p(x, t)$ is assumed to be constant with respect to x (since dx is infinitesimal), $\mathcal{M}(x, t)$ represents the bending moment created by the stress $\sigma_x(x, t)$, and $\mathcal{M}_D(x, t)$ represents the bending moment created by the internal friction force $\sigma_D(x, t)$. As shown in Figure 7 (right) the friction force opposes the strain velocity. That is,

$$\sigma_D(x, t) = C_s \frac{\partial \epsilon_x(x, t)}{\partial t}.$$

Consequently, using (4) and (6) $\mathcal{M}_D(x, t)$ can be derived as follows.

$$\mathcal{M}_D(x, t) = - \int_{A(x)} \sigma_D(x, t) z dA = \int_{A(x)} C_s \frac{d\kappa(x, t)}{dt} z^2 dA = C_s I(x) \frac{\partial^3 w(x, t)}{\partial x^2 \partial t}, \quad (8)$$

where, as before, $w(x, t)$ represents the deflection of the beam's neutral axis at position x and time t .

Figure 7 (left) shows two additional forces acting over the cantilever segment: $f_I(x, t)$, the total inertial forces acting over the differential section (D'Alembert's principle [2]), and $f_D(x, t)$, the distributed external friction force. The former is given by

$$f_I(x, t) = \rho A(x) dx \frac{\partial^2 w(x, t)}{\partial t^2},$$

where $\rho A(x) dx$ is the mass of the cantilever segment. Similarly, the distributed external friction force is given by

$$f_D(x, t) = C(x) \frac{\partial w(x, t)}{\partial x}.$$

The cantilever's EOM can be derived from the dynamic equilibrium equations for both forces and moments. Thus, the equilibrium of forces in the z -axis yields

$$\frac{\partial \mathcal{V}(x, t)}{\partial x} dx = -p(x, t) dx + f_I(x, t) + f_D(x, t) dx,$$

or, equivalently,

$$\frac{\partial \mathcal{V}(x, t)}{\partial x} = -p(x, t) + \rho A(x) \frac{\partial^2 w(x, t)}{\partial t^2} + C(x) \frac{\partial w(x, t)}{\partial x}. \quad (9)$$

To state the moment equilibrium equation, note that the distributed forces $p(x, t)$ and $f_D(x, t)$ can be replaced by a single force $(p(x, t) - f_D(x, t)) dx$ acting through the center of the segment. Thus, the moment generated by this force is proportional to $(dx)^2$. The same is true for the moment generated by $f_I(x, t)$. Consequently, these terms can be dropped from the moment equilibrium equation yielding

$$\mathcal{V}(x, t) dx - \frac{\partial(\mathcal{M}(x, t) + \mathcal{M}_D(x, t))}{\partial x} dx = 0,$$

or, equivalently,

$$\mathcal{V}(x, t) = \frac{\partial(\mathcal{M}(x, t) + \mathcal{M}_D(x, t))}{\partial x}. \quad (10)$$

This is the so-called **shear-moment equation**. Replacing (10), (7), and (8) into (9) and rearranging the terms yields the **cantilever's equation of motion**

$$\frac{\partial^2}{\partial x^2} \left[EI(x) \frac{\partial^2 w(x, t)}{\partial x^2} + C_s I(x) \frac{\partial^3 w(x, t)}{\partial x^2 \partial t} \right] + \rho A(x) \frac{\partial^2 w(x, t)}{\partial t^2} + C(x) \frac{\partial w(x, t)}{\partial x} = p(x, t). \quad (11)$$

There is no closed-form analytical solution for the general form of this equation. However, a simple solution can be formulated for prismatic beams, under the simplifying Assumptions 7 and 8. Thus, in the sequel, $I(x) = I$ and $A(x) = A$. The frictionless case is analyzed first.

3.1.1 Solution of the Frictionless EOM

Without friction ($C_s = C = 0$), the *homogeneous* EOM of a prismatic cantilever is given by

$$EI \frac{\partial^4 w(x, t)}{\partial x^4} + \rho A \frac{\partial^2 w(x, t)}{\partial t^2} = 0. \quad (12)$$

This equation can be easily solved by assuming that $w(x, t) = \phi(x)z(t)$, which yields

$$\frac{\phi^{iv}(x)}{\phi(x)} = -\frac{\rho A \ddot{z}(t)}{EI z(t)},$$

with $\phi^{iv}(x) \triangleq \frac{d^4 \phi(z)}{dx^4}$ ¹. Note that each side of the equation above depends on a different independent variable. Consequently, they must both be equal to a constant, say β^4 , which

¹For any differentiable function $f(x)$ and Roman numeral ℓ , $f^\ell(x) = \frac{d^\ell f(x)}{dx^\ell}$

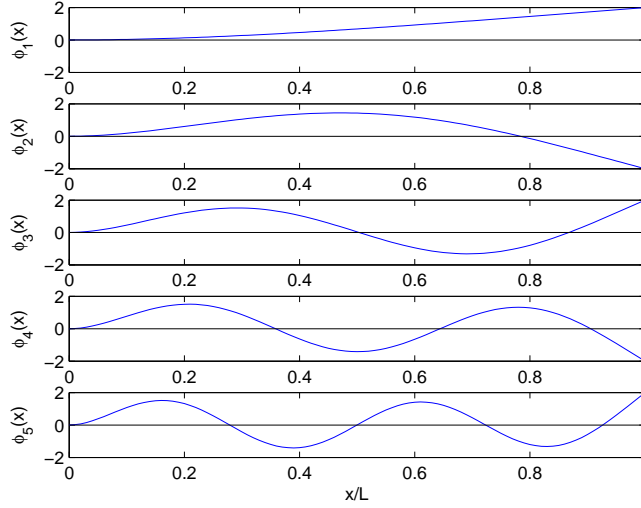


Figure 8. The first five (vibration) mode shape functions. The horizontal axis is normalized, so the shapes are independent of the beam's length.

allows one to split the the partial differential equation into two ordinary differential equations (ODE's)

$$\left. \begin{aligned} \phi^{iv}(x) - \beta^4 \phi(x) &= 0 \\ \ddot{z}(t) + \omega^2 z(t) &= 0, \end{aligned} \right\} \quad (13)$$

where

$$\omega^2 = \frac{\beta^4 EI}{\rho A}. \quad (14)$$

Note that the top equation in (13) determines the *shape* that the cantilever takes while vibrating, while the bottom equation determines the time-varying *amplitude* of the vibration. Six initial conditions are required to solve (13). Two of them, $z(0)$ and $\dot{z}(0)$, can be arbitrarily chosen. Moreover, a simple analysis shows that

$$z(t) = A \cos(\omega t + \varphi), \quad (15)$$

where $\varphi = \arccos(z(0)/A)$ and $A = \sqrt{z^2(0) + (\dot{z}(0)/\omega)^2}$. Clearly, ω determines the natural frequency of oscillation associated with the shape $\phi(x)$. This shape is determined by the remaining four initial conditions, which are set by the cantilever's physical constraints: for all t

$$w(0, t) = 0, \quad \left. \frac{\partial w(x, t)}{\partial x} \right|_{x=0} = 0, \quad \mathcal{M}(L, t) = 0, \quad \text{and} \quad \mathcal{V}(L, t) = 0. \quad (16)$$

This is equivalent to requiring that $\phi(0) = \phi^i(0) = \phi^{ii}(L) = \phi^{iii}(L) = 0$, which leads to the **frequency equation** [4]

$$1 + \cosh(\beta L) \cos(\beta L) = 0. \quad (17)$$

It follows from (17) that β can take any of a countable set of values. The first four can be approximated as follows: $\beta_1 L = 1.8751$, $\beta_2 L = 4.6941$, $\beta_3 L = 7.8548$, and $\beta_4 L = 10.996$.

For $n \geq 5$, $\beta_n L \approx (2n - 1)\pi/2$. Consequently, (13) has countably many solutions of the form [4]

$$\begin{aligned}\phi_n(x) &= \cosh(\beta_n x) - \cos(\beta_n x) - \frac{\cosh(\beta_n L) + \cos(\beta_n L)}{\sinh(\beta_n L) + \sin(\beta_n L)} (\sinh(\beta_n x) - \sin(\beta_n x)) \\ z_n(t) &= A_n \cos(\omega_n t + \varphi_n),\end{aligned}\tag{18}$$

where ω_n, β_n, A_n , and φ_n are related as in (14) and (15). The first five mode shape functions are shown in Figure 8. Note from the linearity of the differential operator that the complete solution of (12), $w(x, t)$, is given by

$$w(x, t) = \sum_{n=1}^{\infty} \phi_n(x) z_n(t).\tag{19}$$

The mode shape functions have two important properties. The first can be proven analytically (see [4])

$$\int_0^L \phi_i(x) \phi_j(x) dx = 0,\tag{20}$$

for every $i, j = 1, 2, \dots, i \neq j$. The second has been demonstrated only numerically and is stated as a conjecture.

Conjecture 3.1 *Consider equation (18). For any $n = 1, 2, \dots$ it follows that*

$$\int_0^L [\phi_i(x)]^2 dx = L.\tag{21}$$

This conjecture is the basis of the Ritz-Galerkin method, which in turn is the basis for the finite element method, and leads to the following observation.

Remark 3.1 *It follows from (20) and (21) that the functions $\phi_n(x)$ form an orthogonal basis of the space $\mathcal{L}^2[0, L]$ (the space of continuous functions over the interval $[0, L]$). Consequently, for any continuous function $f : [0, L] \rightarrow \mathbb{R}$*

$$f(x) = \sum_{n=0}^{\infty} f_n \phi_n(x),$$

where

$$f_n = \int_0^L \phi_n(x) f(x) dx.$$

As will be shown later, these properties are essential for the analysis of a cracked cantilever beam. The next subsection analyzes the cantilever's EOM considering friction.

3.1.2 Solution of the EOM including Friction

Under Assumptions 7 and 8, the EOM (11) for a prismatic beam is given by

$$EI \frac{\partial^4 w(x, t)}{\partial x^4} + a_1 EI \frac{\partial^5 w(x, t)}{\partial x^4 \partial t} + \rho A \frac{\partial^2 w(x, t)}{\partial t^2} + a_0 \rho A \frac{\partial w(x, t)}{\partial x} = p(x, t).$$

Assuming that $w(x, t)$ has the form (19) and using (13) it follows that

$$\sum_{l=1}^{\infty} [EI\beta_l^4 \phi_l(x) z_l(t) + a_1 EI\beta_l^4 \phi_l(x) \dot{z}_l(t) + \rho A \phi_l(x) \ddot{z}_l(t) + a_0 \rho A \phi_l(x) z_l(t)] = p(x, t).$$

After multiplying both sides of the equation above by $\phi_n(t)$, integrating, and using (20) and (21), it follows that

$$\ddot{z}_n(t) + (a_0 + a_1 \omega_n^2) \dot{z}_n(t) + \omega_n^2 z_n(t) = p_n(t), \quad (22)$$

where

$$p_n(t) = \frac{1}{\rho AL} \int_0^L \phi_n(x) p(x, t) dx,$$

is the **generalized load** for the n -th shape function. To solve for $z_n(t)$, apply the Laplace transform to both sides of (22) to obtain

$$(s^2 + 2\xi_n \omega_n s + \omega_n^2) Z_n(s) = z_n(0)(s + 2\xi_n \omega_n) + \dot{z}_n(0) + P_n(s),$$

where $\xi_n \triangleq a_0/2\omega_n + a_1\omega_n/2$, $Z_n(s) = \mathcal{L}\{z_n(t)\}$, $P_n(s) = \mathcal{L}\{p_n(t)\}$, and \mathcal{L} is the Laplace operator. Rearranging this equation, it is easy to show that

$$z_n(t) = \underbrace{\mathcal{L}^{-1} \left\{ \frac{z_n(0)(s + 2\xi_n \omega_n)}{s^2 + 2\xi_n \omega_n s + \omega_n^2} \right\}}_{z_n^h(t)} + \underbrace{\mathcal{L}^{-1} \left\{ \frac{\dot{z}_n(0)}{s^2 + 2\xi_n \omega_n s + \omega_n^2} \right\}}_{z_n^f(t)} + \underbrace{\mathcal{L}^{-1} \left\{ \frac{P_n(s)}{s^2 + 2\xi_n \omega_n s + \omega_n^2} \right\}}_{z_n^f(t)}.$$

where $z_n^h(t)$ and $z_n^f(t)$ are, respectively, the homogeneous and forced responses. The homogeneous response is given by

$$z_n^h(t) = \left[\frac{z(0)\omega_n}{\varpi_n} \cos(\varpi_n t - \psi_n) + \frac{\dot{z}_n(0)}{\varpi_n} \sin(\varpi_n t) \right] \exp(-\xi_n \omega_n t), \quad (23)$$

where $\varpi_n \triangleq \omega_n \sqrt{1 - \xi_n^2}$, $\psi_n \triangleq \arctan^{-1} \left(\frac{\xi_n}{\sqrt{1 - \xi_n^2}} \right)$, and $u(t)$ represents the unit step function.

The forced response depends on the specific loading function $p(x, t)$. Thus, the following extra assumption is needed.

A10 The beam is subject to the load created by its own weight and by a point force, $\ell(t)$, acting on its free end. That is,

$$p(x, t) = \rho Ag[u(x) - u(x - L)]u(t) + \mathbf{1}_{\{x=L\}}\ell(t),$$

where $\mathbf{1}_{\{x=L\}}$ is the indicator function over $x = L$, and $u(t)$ is included for mathematical convenience.

Under this assumption the generalized loads, $p_n(t)$, can be computed as follows

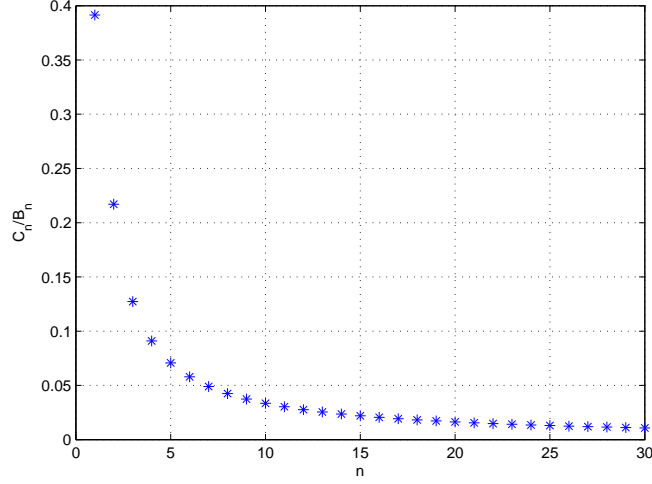


Figure 9. Plot of $C_n/B_n L$ as a function of n .

$$\begin{aligned}
p_n(t) &= \frac{1}{\rho AL} \int_0^L [\rho Ag[u(x) - u(x-L)]u(t) + \mathbf{1}_{\{x=L\}}\ell(t)]\phi_n(x)dx \\
&= \frac{g}{L}u(t) \int_0^L \phi_n(x)dx + \frac{\ell(t)}{\rho AL} \int_0^L \mathbf{1}_{\{x=L\}}\phi(x)dx \\
&= 2g \frac{C_n}{\beta_n L} u(t) + \phi_n(L) \frac{\ell(t)}{\rho AL} \\
&= 2g \frac{C_n}{\beta_n L} u(t) + 2(-1)^{n-1} \frac{\ell(t)}{\rho AL},
\end{aligned}$$

with $C_n \triangleq (\cosh(\beta_n L) + \cos(\beta_n L))/(\sinh(\beta_n L) + \sin(\beta_n L))$. Note that $C_n/B_n L$ decays rapidly to zero as n increases (see Figure 9). Moreover, the first four values are 0.3915, 0.2170, 0.1272, and 0.0909, which suggest that the cantilever's weight has limited influence on the cantilever's vibration for high vibration modes.

For detection purposes (see Section 4), the point force $\ell(t)$ will be set to $\ell(t) = \sin(\omega t)u(t)$, which yields

$$p_n(t) = 2g \frac{C_n}{\beta_n L} u(t) + \frac{2(-1)^{n-1}}{\rho AL} \sin(\omega t)u(t),$$

and

$$P_n(s) = 2g \frac{C_n}{\beta_n L} \frac{1}{s} + \frac{2(-1)^{n-1}}{\rho AL} \frac{\omega}{s^2 + \omega^2}.$$

Thus, the forced solution is given by

$$\begin{aligned}
z_n^f(t) &= \frac{2gC_n}{\omega_n^2 \beta_n L} [1 - \exp(-\xi_n \omega_n t) \cos(\varpi_n t - \psi_n)] \\
&\quad + \frac{2(-1)^{n-1}}{\rho AL \sqrt{(\omega^2 - \omega_n^2)^2 + (2\xi_n \omega_n \omega)^2}} [\sin(\omega t + \varphi_n) + \exp(-\xi_n \omega_n t) \sin(\varpi_n t + \varrho_n)] \quad (24)
\end{aligned}$$

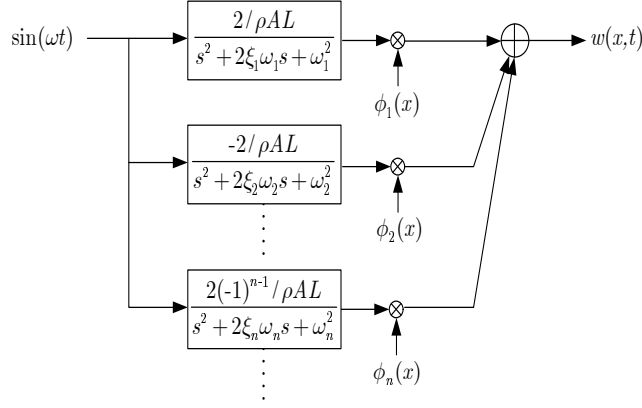


Figure 10. Cantilever representation appropriate for simulation.

with $\varphi_n = \text{atan}(2\xi_n\omega_n\omega/(\omega^2 - \omega_n^2))$ and $\varrho_n = \text{atan}(2\xi_n\omega_n\omega_{dn}/(2\xi_n^2\omega_n^2 + \omega^2 - \omega_n^2))$. It can be shown from the physical data provided in [5] that the first five values of $1/\omega_n^2$ are $5.43765e-3$, $0.13845e-3$, $0.01766e-3$, $0.0045988e-3$, and $0.0016829e-3$. This and Figure 9 clearly indicate that the cantilever's weight only plays a role on the first mode of vibration. Moreover, as a first approximation, it may be completely ignored, which is the approach followed in the sequel.

3.1.3 Simulation of the Equation of Motion

There are at least two methods available to simulate an undamaged vibrating cantilever using the theory presented so far. For example, when very precise results are needed the partial differential equation (11) can be solved using specialized numerical software packages. On the other hand, when approximate results are acceptable it is simpler to simulate a truncated version of (19). To do so, let $W(x, s) \triangleq \mathcal{L}\{w(x, t)\}$ and observe that

$$W(x, s) \approx \sum_{n=1}^{N_t} \phi_n(x) Z_n(s),$$

for a large $N_t \in \mathbb{Z}^+$. Assuming zero initial conditions and disregarding the effect of the cantilever's weight, this equation can be written as

$$W(x, s) \approx \mathcal{L}\{\sin(\omega t)u(t)\} \sum_{n=1}^{N_t} \phi_n(x) \frac{2(-1)^{n-1}/\rho AL}{s^2 + 2\xi_n\omega_n s + \omega_n^2}.$$

Moreover, defining $H_n(x, s)$, $n = 1, 2, \dots$, and $H(x, s)$ as

$$\begin{aligned} H_n(x, s) &\triangleq \frac{2(-1)^{n-1}/\rho AL}{s^2 + 2\xi_n\omega_n s + \omega_n^2} \\ H(x, s) &\triangleq \sum_{n=1}^{\infty} \phi_n(x) H_n(x, s), \end{aligned} \tag{25}$$

it is easy to show that

$$w(x, t) = h(x, t) * \sin(\omega t),$$

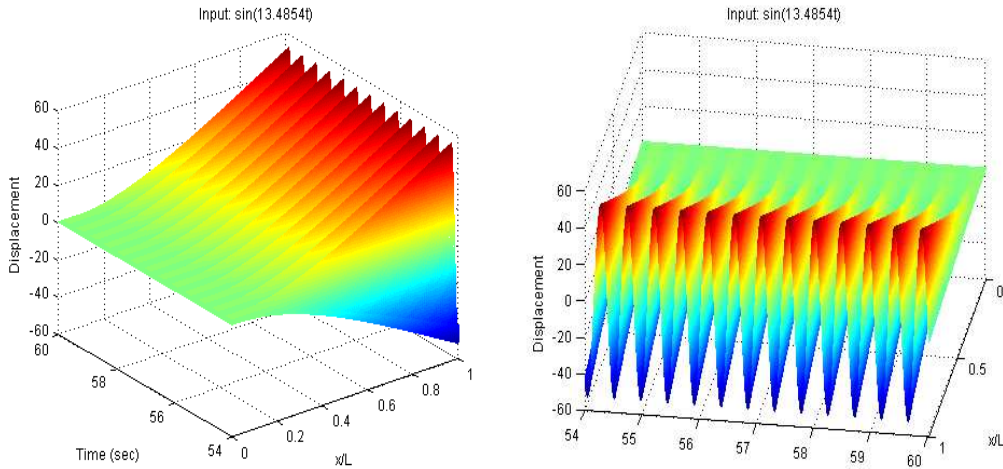


Figure 11. Output of the programs DATA4SIM_CANTILEVER.m and SHAPE_CANTILEVER.mdl. The cantilever is loaded with $\ell(t) = \sin(13.4854t)$, which excites (only) the first natural oscillation mode.

where $h(x, t) = \mathcal{L}^{-1}\{H(x, s)\}$ and $*$ denotes the convolution operator. Thus, the vibrations $w(x, t)$ can be interpreted as the response of the linear system $h(x, t)$ to the input $\sin(\omega t)$, where $h(x, t)$ represents the cantilever's internal dynamics. Alternatively, (25) suggests that the cantilever is a distributed system [6] formed by the weighted parallel composition of countably many second order systems (one for each vibration mode), with weighting functions $\phi_n(x)$. This interpretation is shown graphically in Figure 10.

This approach can be easily implemented in Matlab $\text{\textcircled{R}}$ and Simulink $\text{\textcircled{R}}$ by considering a finite number of vibration modes (see Appendix). The programs DATA4SIM_CANTILEVER.m and SHAPE_CANTILEVER.mdl implement this strategy. Figure 11 shows an example of their output.

3.2 The Hu-Washizu-Barr Variational Principle

The variational principle is an alternative method for determining the equation of motion of a physical system, by identifying the conditions under which the variation of a certain functional J , which is related to the energy of the system, is equal to zero. That is, the EOM arises when making $\delta J = 0$. This variation is derived by assuming small changes in the trajectories followed by the physical system. An elegant explanation of this principle can be found in [7], while a more fundamental discussion can be found in [8].

The specific adaptation of this principle for linear elastic mechanical systems was derived independently by Hu [9] and Washizu [10], and was extended by Barr [11], who showed that the variational equation $\delta J = 0$ leads to

$$\begin{aligned}
& \underbrace{\int_V [\sigma_{ij,j} + F_i - \rho \dot{p}_i] \delta u_i dV}_{\text{dynamic-equilibrium}} + \underbrace{\int_V [\sigma_{ij} - W_{,\epsilon_{ij}}] \delta \epsilon_{ij} dV}_{\text{strain-stress}} + \underbrace{\int_V [\epsilon_{ij} - 1/2(u_{i,j} + u_{j,i})] \delta \sigma_{ij} dV}_{\text{strain-displacement}} \\
& + \underbrace{\int_V [\rho \dot{u}_i - \tilde{T}_{,p_i}] \delta p_i dV}_{\text{veloc.-momentum}} + \underbrace{\int_{S_p} [\bar{g}_i - g_i] \delta u_i dS + \int_{S_u} [u_i - \bar{u}_i] \delta g_i dS}_{\text{boundary conditions}} = 0. \quad (26)
\end{aligned}$$

In this equation, each integrand is presented in short-hand notation, where $i, j \in \{x, y, z\}$ are indexes of an implied summation. Thus, for example, the complete velocity-momentum term is given by

$$\begin{aligned}
\int_V [\rho \dot{u}_i - \tilde{T}_{,p_i}] \delta p_i dV & \equiv \int_V \sum_{i \in \{x,y,z\}} [\rho \dot{u}_i - \tilde{T}_{,p_i}] \delta p_i dV \\
& = \int_V \left\{ [\rho \dot{u}_x - \tilde{T}_{,p_x}] \delta p_x + [\rho \dot{u}_y - \tilde{T}_{,p_y}] \delta p_y + [\rho \dot{u}_z - \tilde{T}_{,p_z}] \delta p_z \right\} dV.
\end{aligned}$$

The comma present in some subindexes represents the derivative of the term at the left of the comma with respect to the term on its right, *after replacing i (or j) by x, y or z* . For example: if $i = x$ and $j = z$ then $u_{i,j} = \frac{du_x}{dz}$.

In each term u_i , $i = x, y, z$, denotes displacement of a differential piece of material in the, respectively, x, y , and z directions. Similarly, ϵ_{ij} , σ_{ij} and p_i represent, respectively, strain, stress and velocity components in the indicated planes and directions. ρ , $\tilde{T} = \sum_i \frac{\rho p_i^2}{2}$, and W represent the mass density, kinetic energy density function and the strain energy density function respectively (δ_{ij} is Kronecker's delta). Finally, F_i denotes the body forces and V the total volume of the the mechanical system (the beam) under consideration.

Note that every integral in (26) is multiplied by a variational term (e.g., δu_i , $\delta \epsilon_{ij}$, etc.). Since the variational terms are independent and arbitrary, (26) can only hold if all the integrals are simultaneously zero (for each value of the variational terms' subindexes). Moreover, equating to zero the first four integrals leads to the desired equation of motion, whereas zeroing the remaining two terms, the boundary conditions terms, determines a particular solution for the EOM. The latter, however, falls outside the scope of this report (see [12] for an in depth discussion).

The variational principle approach is both conceptually and computationally demanding. Nevertheless it provides a systematic method to derive the equation of motion associated with a cracked vibrating cantilever as shown in [12] and [13]. These results will be summarized next after demonstrating the variational approach for an undamaged prismatic cantilever beam. The summary will be followed by a discussion on approximate methods for solving the EOM and on simulation issues.

3.2.1 Derivation of the Frictionless Homogeneous EOM using Variational Methods

Consider again the cantilever in Figure 6, disregarding cracks, internal friction forces or loads. For a small deflection in the z -axis it is easy to see that $u_z = w(x, t)$, $u_x = -z \frac{\partial w}{\partial x}$, and $u_y = 0$ [12]. The other components of (26) are set as follows:

$$\begin{aligned}
\epsilon_{xx} = \epsilon_x = -zS(x, t), \quad \epsilon_y = \epsilon_z = -\nu\epsilon_x, \quad \epsilon_{ij} = 0, i \neq j \\
\sigma_{xx} = \sigma_x = -zT(x, t), \quad \sigma_y = \sigma_z = \sigma_{xy} = \sigma_{yz} = 0, \quad \sigma_{xz} = \sigma_{xz}(x, z, t), \\
p_x = 0, \quad p_y = 0, \quad p_z = P(x, t), \\
F_x = 0, \quad F_y = 0, \quad F_z = 0,
\end{aligned}$$

where ν is Poisson's ratio (see Section 2) and S, T, P, w are unknown functions (the meaning of this choice of parameters can be found in, for instance, [8]). Note that $\sigma_{xz} \neq 0$ to allow for the loading of the beam. To obtain the EOM, these parameters should be put back into (26) and each term should be equated to zero, as shown next.

Strain-Displacement Term

Observe from the conditions above that $\epsilon_{ij} - \frac{1}{2}(u_{i,j} + u_{j,i}) = 0$ when $i \neq j$. Consequently, only variations of the form $\delta\sigma_{ii}$ should be considered. Since $\sigma_y = \sigma_z = 0$, the only available strain variation is $\delta\sigma_{xx} = -z\delta T$ (z is not an independent variation variable). Consequently

$$\begin{aligned}
\int_V [\epsilon_{ij} - 1/2(u_{i,j} + u_{j,i})] \delta\sigma_{ij} dV &= \int_V - \left[\epsilon_{xx} - \frac{du_x}{dx} \right] z \delta T dV \\
&= \int_V \left[z^2 S(x, t) - z^2 \frac{\partial^2 w(x, t)}{\partial x^2} \right] dV \delta T \\
&= \int_x \left(S(x, t) \int_A z^2 dA - \frac{\partial^2 w(x, t)}{\partial x^2} \int_A z^2 dA \right) dx \delta T.
\end{aligned}$$

Since $I = \int_A z^2 dA$ is constant for an undamaged prismatic beam, equating to zero the strain-displacement term yields

$$S(x, t) = \frac{\partial^2 w(x, t)}{\partial x^2}. \quad (27)$$

Strain-Stress Term

First, note from the preceding discussion that $\delta\epsilon_{ij} = 0$ for $i \neq j$. Next, observe that W is given by [8, page 27]

$$W = \frac{E\nu}{2(1+\nu)(1-2\nu)} (\epsilon_x + \epsilon_y + \epsilon_z)^2 + G(\epsilon_x^2 + \epsilon_y^2 + \epsilon_z^2) + G(\epsilon_{xy}^2 + \epsilon_{xz}^2 + \epsilon_{yx}^2)$$

where E and G are defined in (1). Consequently, it is not difficult to show that

$$W_{,\epsilon_{xx}} = W_{,\epsilon_x} = -zES(x, t), \quad W_{,\epsilon_y} = W_{,\epsilon_z} = 0.$$

This and the condition $\sigma_y = \sigma_z = 0$ yield

$$\begin{aligned}
\int_V [\sigma_{ij} - W_{,\epsilon_{ij}}] \delta\epsilon_{ij} dV &= \int_V [\sigma_x - W_{,\epsilon_x}] dV \delta\epsilon_x \\
&= \int_x \left(T(x, t) \int_A z^2 dA - ES(x, t) \int_A z^2 dA \right) dx \delta S,
\end{aligned}$$

which, after equating it to zero, implies that

$$T(x, t) = ES(x, t). \quad (28)$$

Thus, $\sigma_x = E\epsilon_x$ as expected.

Velocity-Momentum Term

It follows from the conditions stated above that only $\delta p_x = \delta P$ is relevant. Also note that $\frac{\partial \tilde{T}}{\partial p_x} = \rho p_x = \rho P(x, t)$. Thus,

$$\begin{aligned} \int_V [\rho \dot{u}_i - \tilde{T}_{,pi}] \delta p_i dV &= \int_V [\rho \dot{u}_x - \tilde{T}_{,px}] dV \delta P \\ &= \int_x \left(\frac{\partial w(x, t)}{\partial t} \int_A \rho dA - P \int_A \rho dA \right) dx \delta P. \end{aligned}$$

Moreover, since $m = \int_A \rho dA$ is constant, it follows after equating this term to zero that

$$P = \frac{\partial w(x, t)}{\partial t}. \quad (29)$$

Dynamical Equilibrium Term

First, note that $\delta u_y = 0$ and that the body forces are zero. That is, $F_i = 0$, $i = x, y, z$. Consequently,

$$\int_V [\sigma_{ij,j} + F_i - \rho \dot{p}_i] \delta u_i dV = \int_V \left[\frac{\partial \sigma_x}{\partial x} + \frac{\partial \sigma_{xz}}{\partial z} \right] dV \delta u_x + \int_V \left[\frac{\partial \sigma_{zx}}{\partial x} - \rho \frac{\partial P(x, t)}{\partial t} \right] dV \delta w$$

Since it can be shown that $\delta u_x = -z \delta \left(\frac{\partial w(x, t)}{\partial t} \right) = \frac{\partial \delta w}{\partial x}$ (c.f. [7]), it follows that

$$\int_V [\sigma_{ij,j} + F_i - \rho \dot{p}_i] \delta u_i dV = \int_V \left[z^2 \frac{\partial T}{\partial x} - z \frac{\partial \sigma_{xz}}{\partial z} \right] \frac{\partial \delta w}{\partial x} dV + \int_V \left[\frac{\partial \sigma_{zx}}{\partial x} - \rho \frac{\partial P(x, t)}{\partial t} \right] dV \delta w.$$

The preceding equality yields, after applying integration by parts twice (see [12, page 642]) and rearranging terms, the following expression

$$\begin{aligned} \int_V [\sigma_{ij,j} + F_i - \rho \dot{p}_i] \delta u_i dV &= \underbrace{\int_A \left[z^2 \frac{\partial T(x, z)}{\partial x} - z \frac{\partial \sigma_{xz}}{\partial z} \delta w \right] \Big|_x + \int_y \int_z \frac{\partial z \sigma_{xz}}{\partial x} dx dy \delta w \Big|_z}_{\text{additional boundary conditions}} \\ &\quad - \int_x \left(\frac{\partial P(x, t)}{\partial t} \int_A \rho dA + \frac{\partial^2 T(x, t)}{\partial x^2} \int_A z^2 dA \right) dx \delta w. \end{aligned}$$

Thus, equating the dynamical equilibrium term to zero yields two additional boundary conditions and the following equation

$$\rho A \frac{\partial P(x, t)}{\partial t} + I \frac{\partial^2 T(x, t)}{\partial x^2} = 0. \quad (30)$$

Finally, replacing (27)-(29) into (30) yields

$$EI \frac{\partial^4 w(x, t)}{\partial x^4} + \rho A \frac{\partial^2 w(x, t)}{\partial t^2} = 0$$

as expected (see Section 3.1.1). The next section summarizes the use of this technique to derive the EOM associated with cracked cantilevers.

3.2.2 Derivation of the EOM Associated with a Cracked Cantilever Using Variational Methods

As will be explained in more detail in Section 4, determining the mode shape functions for a cracked cantilever is necessary for fault detection. This requires one to first derive the EOM associated with a cracked cantilever and then find its solution.

Deriving the EOM depends on the assumed crack behavior: The cracks can either open and close while the cantilever vibrates [14, 15] or remain open [12, 13]. Under the latter approach, the cantilever's behavior remains linear, leading to a simpler analysis. This approach is summarized next.

Consider again the cantilever in Figure 6, disregarding the internal friction forces. As pointed out in [12], the presence of cracks leads to changes in stress and strain distributions in the area around the cracked section. Moreover, the stress distribution is non-uniform, peaking near the crack tip. Since the stress distribution function is unknown, the author modeled it as a function $f(x, z)$ that attains its maximum at the crack tip and decays with the distance from the crack plane. This function only affects σ_x (and ϵ_x) and can be estimated experimentally [12] or numerically via finite element analysis [13]. This setup can be analyzed using the variational method considering

$$\begin{aligned} \epsilon_x &= [-z + f(x, t)]S(x, t), & \epsilon_y &= \epsilon_z = -\nu\epsilon_x, & \epsilon_{ij} &= 0, i \neq j \\ \sigma_x &= [-z + f(x, t)]T(x, t), & \sigma_y &= \sigma_z = \sigma_{xy} = \sigma_{yz} = 0, & \sigma_{xz} &= \sigma_{xz}(x, z, t), \\ p_x &= 0, & p_y &= 0, & p_z &= P(x, t), \\ F_x &= 0, & F_y &= 0, & F_z &= 0. \end{aligned}$$

Repeating the procedure summarized in the subsection 3.2.1 yields the following EOM [12].

$$\begin{aligned} E[I - K(x)]Q(x)\frac{\partial^4 w(x, t)}{\partial x^4} + 2E [Q^i(x)[I - K(x)] - K^i(x)Q(x)]\frac{\partial^3 w(x, t)}{\partial x^3} \\ + E [Q^{ii}(x)[I - K(x)] - K^i(x)Q^i(x) - K^{ii}(x)Q(x)]\frac{\partial^2 w(x, t)}{\partial x^2} + \rho A\frac{\partial^2 w(x, t)}{\partial t^2} = 0, \end{aligned} \quad (31)$$

where

$$K(x) = \int_A z f(x, z) dA, \quad L(x) = \int_A f^2(x, z) dA, \quad Q(x) = \frac{I - K(x)}{I - 2K(x) + L(x)},$$

and the boundary conditions are give by

$$w(0, t) = \frac{\partial w(x, t)}{\partial x} \Big|_{x=0} = 0 = \frac{\partial^2 w(x, t)}{\partial x^2} \Big|_{x=L} = \frac{\partial^3 w(x, t)}{\partial x^3} \Big|_{x=L} = 0. \quad (32)$$

$$(33)$$

For a cantilever with the geometry shown in Figure 6, $f(x, t)$ can take the forms explained next [12, 13].

Single-edge cracks: For a prismatic beam with one single-edge crack, $f(x, z)$ is given by

$$f(x, z) = \left[z - \frac{I}{I_r + 0.5aI_c}(z + 0.5a)u(D - a - z) \right] \exp\left(-\frac{\alpha|x - x_c|}{D}\right),$$

where a is the crack's depth, x_c is the crack's location,

$$I = \frac{4BD^3}{3}, \quad I_r = \int_{A_{\text{crack}}} z^2 dA = \frac{2B((D-a)^3 + D^3)}{3}, \quad I_c = \int_{A_{\text{crack}}} z dA = aB(a-2D),$$

(A_{crack} denotes the area of the cracked cross-section), and $\alpha = 1.276$ is a numerically estimated dimensionless parameter [13]. It follows from this expression that

$$Q(x) = \left(1 + \left(\frac{I - I_r - 0.5aI_c}{I_r + 0.5aI_c} \right) \exp \left(-2 \frac{\alpha |x - x_c|}{D} \right) \right)^{-1}.$$

A similar derivation can be done for a beam with N_c single-edge cracks. In such cases $f(x, z)$ is given by

$$f(x, z) = \sum_{i=1}^{N_c} \left[z - \frac{I}{I_{r_i} + 0.5a_i I_{c_i}} (z + 0.5a_i) u(D - a_i - z) \right] \exp \left(-\frac{\alpha_i |x - x_{c_i}|}{D} \right),$$

where $a_i, x_i, I_{r_i}, I_{c_i}$, and $\alpha_i, i = 1, \dots, N_c$ are the parameters related to each crack.

Double-edge cracks:

$$f(x, z) = \left[z - \frac{I}{I_r} z (u(z + D - a) - u(z - D + a)) \right] \exp \left(-\frac{\alpha |x - x_c|}{D} \right).$$

In this case, it is easy to show that $I/I_r = D^3/(D-a)^3$. Consequently,

$$Q(x) = \left(1 + \left(\frac{D^3 - (D-a)^3}{(D-a)^3} \right) \exp \left(-2 \frac{\alpha |x - x_c|}{D} \right) \right)^{-1}.$$

As before, $Q(x)$ can also be derived for multiple double-edge cracks by observing that in such cases

$$f(x, z) = \sum_{i=1}^{N_c} \left[z - \frac{I}{I_{r_i}} z (u(z + D - a_i) - u(z - D + a_i)) \right] \exp \left(-\frac{\alpha_i |x - x_{c_i}|}{D} \right).$$

Since in all cases $K(x) = 0$, the EOM can be simplified as follows

$$EIQ(x) \frac{\partial^4 w(x, t)}{\partial x^4} + EIQ^i(x) \frac{\partial^3 w(x, t)}{\partial x^3} + EIQ^{ii}(x) \frac{\partial^2 w(x, t)}{\partial x^2} + \rho A \frac{\partial^2 w(x, t)}{\partial t^2} = 0. \quad (34)$$

Finally, note that these results have been refined using more detailed crack models [16].

3.2.3 Solution of the EOM Associated with a Cracked Cantilever

To find a solution for the simplified EOM (34), assume as before that $w(x, t) = \phi_c(x)z(t)$. This leads to

$$\frac{Q(x)\phi_c^{iv}(x) + Q^i(x)\phi_c^{iii}(x) + Q^{ii}(x)\phi_c^{ii}(x)}{\phi_c(x)} = -\frac{\rho A \ddot{z}(t)}{EI z(t)},$$

which leads to two ordinary differential equations

$$Q(x)\phi_c^{iv}(x) + Q^i(x)\phi_c^{iii}(x) + Q^{ii}(x)\phi_c^2(x) - \beta_c^4\phi_c(x) = 0 \quad (35)$$

$$\ddot{z}(t) + \omega_c^2 z(t) = 0, \quad (36)$$

with

$$\omega_c^2 = \beta_c^4 \frac{EI}{\rho A}.$$

The initial conditions for (36), $z(0)$ and $\dot{z}(0)$, can be chosen arbitrarily. The boundary conditions for (35) are given in (32). That is, $\phi_c(0) = \phi_c^i(0) = \phi_c^{ii}(L) = \phi_c^{iii}(L) = 0$. Equation (36) is solved as in (15) once β_c is determined. Equation (35), however, is an ODE with varying parameters and cannot be solved with the approach that led to (18). It must be solved using series methods (c.f. [17]). Under the assumption of convergence, $\phi_c(x)$ can be expressed as

$$\phi_c(x) = \sum_{i=1}^{\infty} \mu_i g_i(x), \quad (37)$$

where $g_i(x)$, $i = 1, 2, \dots$, constitute a series of known (and arbitrary) functions that are easy to manipulate. Usually, $g_i(x) = x^i$, which leads to the power series solution $\phi_c(x) = \sum_{i=1}^{\infty} \mu_i x^i$. Substituting this series into (35) yields (at most) a fourth order difference equation for the coefficients μ_i . This equation can then be uniquely solved by employing the initial conditions (32). Unfortunately, this technique requires to either compute countably many coefficients μ_i (a closed-form solution for $\phi_c(x)$ is not always available) or truncate the series, introducing the need of estimating the truncation error, which is not always possible.

An alternative technique is the Ritz-Galerkin method [18], which reduces solving (35) to solving a finite set of linear equations. The method produces only approximated solutions. However, the approximation error can always be computed, and it is shown to decrease as the number of linear equations increases. Note that any solution of (35), $\phi_c(x)$, lies in $\mathcal{L}^2[0, 1]$. Recall from Conjecture 3.1 that $\phi_n(x)$, $n = 1, \dots$, form a basis of $\mathcal{L}^2[0, L]$. The Ritz-Galerkin method states that good approximations of $\phi_c(x)$ lie in finite subspaces of $\mathcal{L}^2[0, 1]$. For instance, let $\mathcal{S} = \text{span}\{\phi_1(x), \dots, \phi_N(x)\}$ (a subspace of $\mathcal{L}^2[0, 1]$) and observe that it may contain several approximated solutions. Let $\hat{\phi}_{c_l}(x)$ denote the l -th approximated solution and observe that

$$\hat{\phi}_{c_l}(x) = \sum_{i=1}^N \mu_i^l \phi_i(x), \quad (38)$$

for a particular set of coefficients μ_1^l, \dots, μ_N^l . Substituting this expression into (35) leads to

$$\sum_{i=1}^N \mu_i^l [Q(x)\phi_i^{iv}(x) + Q^i(x)\phi_i^{iii}(x) + Q^{ii}(x)\phi_i^{ii}(x)] = \beta_c^4 \sum_{i=1}^N \mu_i^l \phi_i(x).$$

Multiplying both sides by $\phi_j(x)$, using (13) and (21), and integrating yields

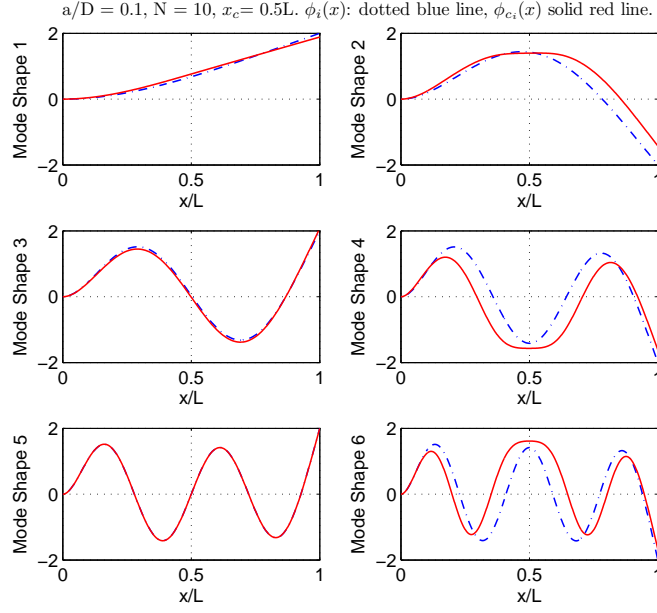


Figure 12. Mode shape functions of an undamaged cantilever (dotted blue line) and a single-edge-cracked cantilever (solid red line). The crack position is $x_c = 0.5L$ and its depth is $a = 0.1D$. The plots were generated using the Ritz-Galerkin method with ten basis ($N=10$).

$$\sum_{i=1}^N \mu_i^l \int_0^L [\beta_i^4 Q(x) \phi_i(x) \phi_j(x) + Q^i(x) \phi_i^{iii}(x) \phi_j(x) + Q^{ii}(x) \phi_i^{ii}(x) \phi_j(x)] dx = \beta_{c_l}^4 L \mu_j^l.$$

If $M_{ji} \triangleq (1/L) \int_0^L [\beta_i^4 Q(x) \phi_i(x) \phi_j(x) + Q^i(x) \phi_i^{iii}(x) \phi_j(x) + Q^{ii}(x) \phi_i^{ii}(x) \phi_j(x)] dx$, $M \triangleq [M_{ji}]$, and $\Gamma_l \triangleq [\mu_1^l, \dots, \mu_N^l]^T$, then the coefficients μ_1, \dots, μ_N can be found by solving the eigen-equation

$$M\Gamma_l = \beta_{c_l}^4 \Gamma_l. \quad (39)$$

Clearly, Γ is an eigenvector of M and β_c^4 is its associated eigenvalue. If one assumes that $\text{rank}(M) = N$, this equation can be interpreted as follows: There are N different solutions for (35), one per each eigenvalue of M . That is, the cracked prismatic cantilever has (at least) N mode shape functions with associated natural frequencies $\omega_{c_l} = \beta_{c_l}^2 \sqrt{\frac{EI}{\rho A}}$, $l = 1, 2, \dots, N$.

Finally, observe from (38) that each solution $\hat{\phi}_{c_l}(x)$ satisfies the boundary conditions (32). Consequently, an approximation of $\hat{w}(x, t)$ can be realized as follows

$$\hat{w}(x, t) = \sum_{l=1}^N \hat{\phi}_{c_l}(x) z_l(t), \quad (40)$$

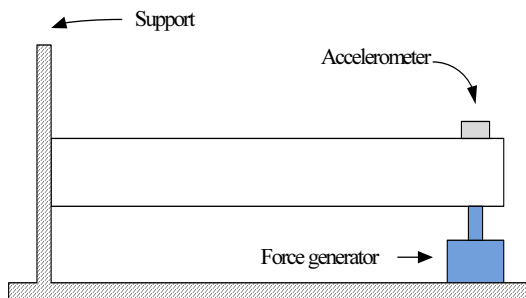


Figure 13. Setup for a frequency-based fault detection test.

where $z_l(t)$ is the solution of (36) with ω_c substituted by ω_{c_l} . Moreover, direct comparison of (40) and (19) shows that the cracked cantilever can be simulated using the same approach explained in Subsection 3.1.3.

The procedure described above has been implemented in the Matlab [®] script COEFFICIENT3.m. An example of its output is shown in Figure 12. The next section discusses different fault detection methods based on the theory presented so far.

4 Fault Detection Methods for Cantilever Beams

There exist several methods for detecting faults in cantilever-like structures, such as oil platforms, buildings, or aircraft and helicopter wings, as evidenced in the surveys [19–21]. Broadly speaking, these methods are classified into two groups: frequency-based methods and mode-shape-based methods. Both are briefly summarized next. The summary is followed by a discussion on a proposed detection scheme suitable for formal verification.

4.1 Frequency-Based Detection Methods

A review of these methods can be found in [22]. In general, these methods exploit the knowledge of the natural frequencies and phases associated with the vibration modes of an undamaged cantilever. Recall that the natural frequencies are obtained from $\omega_n = \beta_n^2 \sqrt{\frac{EI}{\rho A}}$. Thus any change in the cantilever's stiffness, EI , or in its cantilever mass, ρA , leads to a shift in these frequencies. The natural frequencies can be measured with a test setup similar to the one in Figure 13. In this setup, a force generator applies a sinusoidal point load at the free end of a cantilever, while an accelerometer measures $\frac{d^2 w(L,t)}{dt^2}$. Ignoring the cantilever's weight and the transient effects, it is easy to show from (19) and (24) that

$$\frac{d^2 w(L,t)}{dt^2} = \sum_{n=1}^{\infty} \frac{4\omega^2}{\rho AL \sqrt{(\omega^2 - \omega_n^2)^2 + (2\xi_n \omega_n \omega)^2}} \sin(\omega t + \varphi_n).$$

This equation suggests that the natural frequencies can be found one at a time by varying the load frequency ω and filtering the accelerometer's signal with a band-pass filter. For instance, to find ω_1 , ω should be varied in the neighborhood of $\beta_1^2 \sqrt{\frac{EI}{\rho A}}$. If a band-pass filter around the ideal value of ω_1 is applied, the *real* value of ω_1 can be determined by finding the value of ω that maximizes the filter's output.

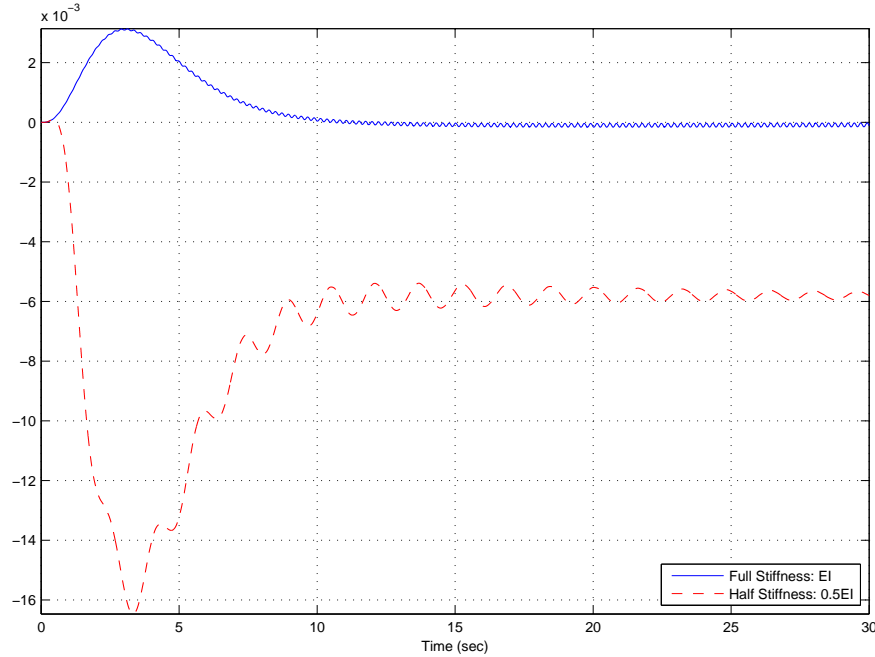


Figure 14. Comparison of fault detector responses using phase measurements: Undamaged cantilever (solid blue) and damaged cantilever (dashed red).

Alternatively, φ_n can be measured by noticing that $\varphi_1 = \pi/2$ when $\omega = \omega_1$. Assuming that the accelerometer's signal is filtered with a low pass filter, it is easy to show that

$$\frac{d^2 w(L, t)}{dt^2} \sin(\omega_1 t) = \frac{1}{\rho A L \xi_1^2 \omega_1^2} [\cos(\pi/2) - \cos(2\omega_1 t + \pi/2)].$$

Thus, applying a second low pass filter to the product above, one should obtain a zero signal. This strategy is simulated in the Simulink[®] model DETECT_CANTILEVER.mdl and an example of its output is shown in Figure 14.

In spite of their simplicity, the major drawback of frequency-based (or phase-based) methods is their low sensitivity to faults. If a fault reduces the cantilever's stiffness by 50%, the natural frequencies are only reduced by 30%. Moreover, as shown in Figure 14 this fault leads to a small change on the detector's output which may not be distinguishable from measurement noise. For a fault introducing a more reasonable 10% stiffness reduction, the natural frequencies are reduced by only 6%, which is virtually indistinguishable from the natural frequency shifts produced by material relaxation [21]. Thus, it is clear that incipient faults, such as a small crack, cannot be effectively detected by these methods.

4.2 Mode-Shaped-Based Detection Methods

These methods perform fault detection by comparing a cantilever's ideal mode shape functions (obtained from physical models) with those estimated from data. The data is usually acquired through a large number of strain sensors positioned along the cantilever's main axis, while the latter oscillates at one its natural frequencies.

Bragg Fiber Optic (FO) strain sensors have been successfully used to perform this type of data acquisition in aircraft wings and other cantilever-type structures [23,24]. These sensors are positioned by embedding a single optical fiber, which contains multiple Bragg gratings, along a cantilever's main axis. As explained in [24], these sensors produce output signals which are proportional to the cantilever's strain at the position where the Bragg gratings are located. It can be shown from (4) and (6) that $\epsilon(x, t) = -D \frac{\partial^2 w(x, t)}{\partial x^2}$. Consequently, (19) yields

$$\frac{\partial^2 \epsilon(x, t)}{\partial x^2} = -D \sum_{n=1}^{\infty} \phi_n(x) (\beta_n^4 z_n(t)).$$

Exciting the cantilever with a sinusoidal force of frequency ω_n yields, after applying a band-pass filter around ω_n ,

$$\frac{\partial^2 \epsilon(x, t)}{\partial x^2} = -\frac{\beta_n^4 D}{\rho A L \xi_n^2 \omega_n^2} \phi_n(x) \cos(\omega_n t).$$

Thus, an estimate of $\phi_n(x)$, $\hat{\phi}_n(x)$, can be obtained by taking multiple sensor readings (every $2\pi/\omega_n$ seconds), averaging the data, and normalizing the results so $\hat{\phi}_n(L) = 2(-1)^{n-1}$. If the natural frequencies ω_n are unknown, they can be estimated by exciting the cantilever with a white noise loading force and analyzing the resulting spectrum of $w(L, t)$, as explained in [25].

Once the mode shape functions are estimated, damage in the cantilever can be detected by direct comparison with the ideal functions, by analyzing changes in the shape function's curvature, or by using other techniques [20,21]. The simplest direct comparison method is the Modal Assurance Criterion (MAC). The MAC is a number between 0 and 1 that quantifies how much the estimated functions $\hat{\phi}_n(x)$ correlate to themselves and to the ideal functions $\phi_n(x)$ [26]. This is done by exploiting properties (20) and (21) as follows

$$\text{MAC} \triangleq \frac{\left(\sum_{i=1}^N \int_0^L \hat{\phi}_n(x) \phi_n(x) dx \right)^2}{\left(\sum_{i=1}^N \int_0^L \hat{\phi}_n^2(x) dx \right) \left(\sum_{i=1}^N \int_0^L \phi_n^2(x) dx \right)}.$$

It follows from this definition that the MAC number reaches 1 only when the estimated shape functions $\hat{\phi}_n(x)$ match perfectly the ideal functions $\phi_n(x)$. Conversely, the closer the MAC is to zero, the more the estimated shape functions differ from the ideal ones. Also note that in practice only a finite number of strain sensors is available. Thus, let N_s denote the number of sensors and assume that they are evenly distributed along the cantilever. Set $\Phi_n = [\phi_n(0), \phi_n(L/N_s), \phi_n(2L/N_s), \dots, \phi_n(L)]$ and $\hat{\Phi}_n = [\hat{\phi}_0, \hat{\phi}_1, \hat{\phi}_2, \dots, \hat{\phi}_{N_s}]$, where $\hat{\phi}_i$ is the (averaged and normalized) output of the strain sensor that yields $\hat{\phi}_n(iL/N_s)$, and note that the MAC can be computed as

$$\text{MAC} = \frac{\left(\sum_{i=1}^N \hat{\Phi}_n \Phi_n^T \right)^2}{\left(\sum_{i=1}^N \|\hat{\Phi}_n\|^2 \right) \left(\sum_{i=1}^N \|\Phi_n\|^2 \right)}.$$

This strategy was implemented in COEFFICIENT3.m and applied to the mode shapes corresponding to the cantilever with a single-edge crack shown in Figure 12 ($x_c = 0.5L$, $a = 0.1D$, and $N = 10$). In this case $\text{MAC} = 0.4981$, clearly indicating the presence of a crack.

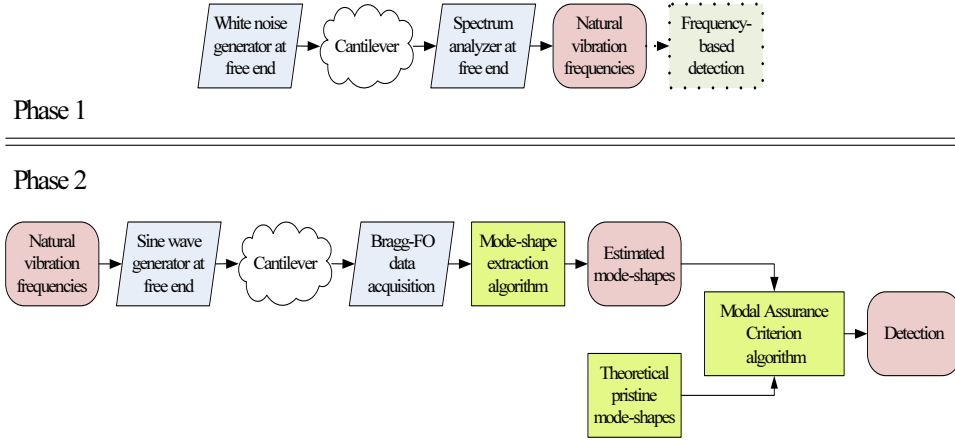


Figure 15. Experimental setup for the proposed mode-shape-based fault detection methodology.

Mode-shape-based methods also present several drawbacks, among which implementation complexity is the major one. Nevertheless, they provide more information than frequency-based methods and are compatible with the Bragg FO sensor technology under development at NASA LaRC [5]. For a more in-depth comparison of frequency-based and mode-shape-based methods see [27].

4.3 A Mode-Shaped-Based Fault Detection Methodology

The proposed methodology consists of the following steps.

- Phase 1
 1. Estimate the cantilever’s natural frequencies of oscillation.
- Phase 2
 2. Apply an external sinusoidal force, so the cantilever vibrates at a prescribed frequency ω . Record vibration data for (at least) $\omega = \omega_1$ and $\omega = \omega_2$.
 3. Estimate from the data (at least) the first two mode-shapes: $\hat{\Phi}_1$ and $\hat{\Phi}_2$.
 4. Compare $\hat{\Phi}_1$ and $\hat{\Phi}_2$ to Φ_1 and Φ_2 using the Modal Assurance Criterion (MAC) or a similar algorithm.
 5. Analyze the results to determine whether a fault is present.

The experimental setup required by this methodology is shown in Figure 15. In this figure, parallelograms represent test equipment, rounded rectangles represent measured/derived data/quantities, and straight rectangles denote formulas and software algorithms that have been explained in this report. Note that the phase 1 natural frequency estimation follows the same procedure described in [25]. Also, note that a software verification testbed for the detection algorithm should also be implemented following the setup in Figure 16.

Many of the Matlab [®] and Simulink [®] scripts required to implements the setups in Figures 15 and 16 have already been implemented. They are listed in the appendix.

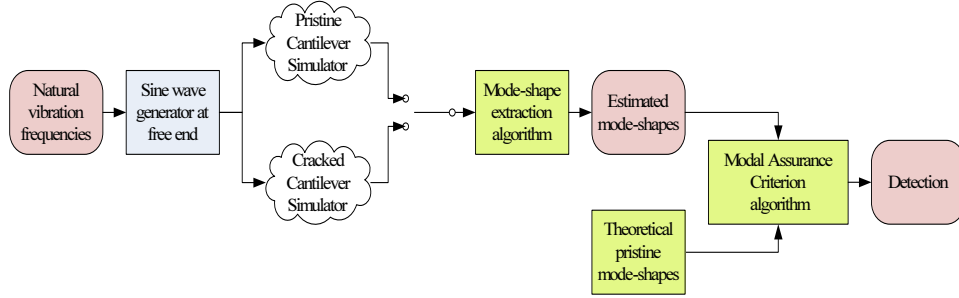


Figure 16. Proposed software verification testbed.

5 Conclusions and Future Research Directions

Summary

This report provided the theoretical framework and basic concepts required to develop and verify fault detection algorithms for cantilever structures, the simplest models for wings. It was implicitly assumed that the faults are detected through vibrational methods. Two different techniques were used to derive the cantilever’s EOM under the assumption of small deflections: dynamic equilibrium, a textbook technique, and the Hu-Washizu-Barr variational principle. The latter is a much more advanced and complex technique that can yield the desired EOM under different crack (fault) conditions. The EOM was solved using classical linear system concepts in combination with the Ritz-Galerkin method. As a result, it was shown how to derive approximate solutions for the EOM (which can be improved to any desired degree of accuracy), which are compatible with standard mode-shape-based fault detection methods described in the literature. In particular, the Modal Assurance Criterion was selected as the detection method of choice because of its simplicity and its compatibility with current NASA LaRC efforts to develop Bragg FO strain sensors for fault detection. Additionally, a complete fault detection methodology has been suggested (leveraging all the concepts introduced in this report), which is compatible with the available technical resources at NASA LaRC and is simple enough to be amenable to formal verification. Finally, many of the software scripts needed for this methodology have been developed and are listed in the Appendix.

Conclusions

- It is clear from the literature that there are no existing methods/technology available for online (or in-flight) fault detection in wing structures.
- Most current fault detection methods require complex testing equipment that, at best, can be carried and installed next to a parked aircraft. Some even require placing the test airplanes in special mounts. This is especially so for frequency-based methods.
- Mode-shape-based methods, specially those using Bragg fiber optic technology, are more suitable to be embedded in aircraft. These methods, however, present several technical challenges:
 - They require precise knowledge of the fault-free (theoretical) wing mode shape functions, which can vary through time due to effects not related to faults (relaxation of material and joints, in-flight mass variation due to fuel depletion). Thus,

the fault-free mode shape functions must be derived experimentally, and there is no obvious technical method to do this.

- Theoretically, to determine the wing mode shape functions, the wings must be excited by a sinusoidal load. This is not compatible with in-flight operation. An alternative could be found by analyzing the forces acting on the wings during flight and determining if they can be modeled as colored noise. In such a case, the EOM becomes a PDE with stochastic inputs, which can be analyzed with available techniques.
- The ability of the Modal Assurance Criterion to self-correlate functions can be assessed mathematically. Additionally, this algorithm is simple to implement numerically. This makes it very attractive for formal verification using tools like PVS.
- Although the physical models and Modal Assurance Criterion presented in this report are well known and widely accepted, there is no obvious way to (mathematically) characterize the discrepancies between the theory and particular wing implementations. This characterization is vital to assess the quality of the detection methods. For instance, there is no clear method to determine the probability of false alarms.
- The results presented in this report constitute a first attempt to solve a complex problem. The work is in its first stages and needs to be developed further following the ideas presented next.

Future Research Directions

- In Section 3, the Hu-Washizu-Barr variational principle was used to derive the EOM of a cantilever with cracks. The resulting EOM is homogeneous. The literature contains several examples of forced EOM derived with this principle, but it is not clear how this is done. This should be explored fully, along with methods to take into consideration internal and external friction forces, since this is required to provide a solid base for cracked cantilever simulations.
- Conjecture 3.1 should be proved mathematically. This is important to correctly justify the use of the MAC for this application.
- A less computationally intensive implementation of the Ritz-Galerkin algorithm must be found
- Explicit estimation error bounds should be found for the Ritz-Galerkin method presented in the Section 3. This is important to formally verify the proposed fault detection methodology.
- A comprehensive analysis and a methodology to formally verify the proposed mode-shape-based fault detection method is needed.
- A complete Matlab/Simulink-based software suite that implements the setup in Figure 16 should be developed.

References

1. C. M. Belcastro, C. L. Allen, Aviation Safety Program – Integrated Vehicle Health Management: Technical plan summary (May 2006).
URL http://www.aeronautics.nasa.gov/nra_pdf/ivhm_tech_plan_c1.pdf
2. A. K. Chopra, Dynamics of Structures: Theory and Applications to Earthquake Engineering, Prentice Hall, Upper Saddle Rive, NJ, 1995.
3. J. M. Gere, Mechanics of Materials, Brooks/Cole-Thomson Learning, Belmont, CA, 2004.
4. R. W. Clough, J. Penzien, Dynamics of Structures, McGraw-Hill, New York, NY, 1975.
5. C. C. Quach, S. L. Vazquez, Panel parameter validation: Internal communication, 2008.
6. H. S. Tzou, L. A. Bergman, Dynamics and Control of Distributed Systems, Cambridge University Press, Cambridge, UK, 1998.
7. H. C. Hu, Variational Principles of Theory of Elasticity with Applications, Gordon and Breach, New York, NY, 1984.
8. K. Washizu, Variational Methods in Elasticity and Plasticity, 3rd Edition, Pergamon Press, Oxford, 1982.
9. H. C. Hu, On some variational principles in the theory of elasticity and plasticity, *Scientia Sinica* 4 (1955) 33–55.
10. K. Washizu, On the variational principles of elasticity and plasticity, Tech. Rep. 25-18, Contract No. N5ori-07833, Massachusetts Institute of Technology, Cambridge, MA (1955).
11. A. D. S. Barr, An extension of the Hu-Washizu variational principle in linear elasticity for dynamic problems, *Trans. ASME. J. Appl. Mechs.* 33 (2) (1966) 465.
12. S. Christides, A. D. S. Barr, One-dimensional theory of cracked Bernoulli-Euler beams, *Int. J. Mech. Sci.* 26 (11/12) (1984) 639–648.
13. M. H. H. Shen, C. Pierre, Free vibrations of beams with a single-edge crack, *Journal of Sound and Vibration* 170 (2) (1994) 237–259.
14. T. G. Chondros, A. D. Dimaragonas, J. Yao, Vibration of a beam with a breathing crack, *Journal of Sound and Vibration* 239 (1) (2001) 57–67.
15. U. Andreaus, P. Casini, F. Vestroni, Non-linear dynamics of a cracked cantilever beam under harmonic excitation, *International Journal of Non-Linear Mechanics* 42 (2007) 566–575.
16. S. H. S. Carneiro, D. J. Inman, Comments on the free vibrations of a beams with a single-edge crack, *Journal of Sound and Vibration* 244 (4) (2001) 729–737.
17. J. K. Hale, Ordinary Differential Equations, Pure and Applied Mathematics, v.21, Wiley-Interscience, New York, NY, 1969.
18. S. C. Brenner, L. R. Scott, The Mathematical Theory of Finite Element Methods, Vol. 15 of Texts in Applied Mathematics, Springer-Verlag, New York, NY, 2008.

19. S. W. Doebling, C. R. Farrar, M. B. Prime, D. W. Shevitz, Damage identification and health monitoring of structural and mechanical systems from changes in their vibration characteristics: A literature review, Tech. Rep. LA-13070-MS, Los Alamos National Laboratory, Los Alamos, NM (1996).
20. S. W. Doebling, C. R. Farrar, M. B. Prime, D. W. Shevitz, A summary review of vibration-based damage identification methods, *Shock and Vibration Digest* 30 (2) (1998) 91–105.
21. E. P. Carden, P. Fanning, Vibration based condition monitoring: A review, *Structural Health Monitoring* 3 (2004) 355–377.
22. O. S. Salawu, Detection of structural damage through changes in frequency: A review, *Engineering Structures* 19 (9) (1997) 718–723.
23. A. Cusano, P. Capoluongo, S. Campopiano, A. Cutolo, M. Giordano, F. Felli, A. Paolozzi, M. Caponero, Experimental modal analysis of an aircraft model wing by embedded fiber bragg grating sensors, *IEEE Sensors J.* 6 (1) (2006) 67–75.
24. P. Capoluongo, C. Ambrosino, S. Campopiano, A. Cutolo, M. Giordano, I. Bovioc, L. Lecce, A. Cusano, Modal analysis and damage detection by fiber Bragg grating sensors, *Sensors and Actuators A* 133 (2007) 415–424.
25. D. F. Jenkins, M. J. Cunningham, W. W. Clegg, M. M. Bakush, Measurement of the modal shapes of inhomogeneous cantilevers using optical beam deflection, *Meas. Sci. Technol.* 6 (2) (1995) 160–166.
26. R. J. Allemang, The modal assurance criterion - twenty years of use and abuse, *Journal of Sound and Vibration* 37 (8) (2003) 14–21.
27. J. T. Kim, Y. S. Ryu, H. M. Cho, N. Stubbs, Damage identification in beam-type structures: Frequency-based method vs mode-shape-based method, *Engineering Structures* 25 (1) (2003) 57–67.

Appendix A

Software Components

The following table describes the main Matlab ® scripts and Simulink ® models that were developed to exercise/test the ideas discussed in this report.

COEFFICIENT3.m	This program calculates the mode shape functions for a cracked cantilever using the Ritz-Galerkin Method. It also implements the MAC algorithm.
PHI.m/HATPHI.m, D2PHI.m, D3PHI.m	Auxiliary scripts that compute, respectively, $\phi_n(x)$ and its second and third derivatives.
DATA4SIM_CANTILEVER.m	This program provides the data required to run the cantilever simulation program, SHAPE_CANTILEVER.mdl. The data provided by the simulator is captured and processed to extract $\hat{\phi}_1(x)$ and $\hat{\phi}_2(x)$ following the procedure explained in Section 4.2.
PLOT_BEAM_SHAPES.m	Auxiliary script that computes and plots the first 'n' mode shape functions of an undamaged cantilever.
Q2.m	Auxiliary script that generates the function $Q(x)$ introduced in Section 3.2.2.
DETECT_CANTILEVER.mdl	Simulation model that performs the phase-based fault detection described in Section 4.1.
N_MODE_CANTILEVER.mdl	Simulation model that recreates the temporal response of a single cantilever vibration mode. To ensure its correct operation the script DATA4SIM_CANTILEVER.m should be executed first.
SHAPE_CANTILEVER.mdl	Simulation model that recreates the complete response of a cantilever beam to a sinusoidal excitation. To ensure its correct operation the script DATA4SIM_CANTILEVER.m should be executed first.

REPORT DOCUMENTATION PAGE			Form Approved OMB No. 0704-0188		
<p>The public reporting burden for this collection of information is estimated to average 1 hour per response, including the time for reviewing instructions, searching existing data sources, gathering and maintaining the data needed, and completing and reviewing the collection of information. Send comments regarding this burden estimate or any other aspect of this collection of information, including suggestions for reducing this burden, to Department of Defense, Washington Headquarters Services, Directorate for Information Operations and Reports (0704-0188), 1215 Jefferson Davis Highway, Suite 1204, Arlington, VA 22202-4302. Respondents should be aware that notwithstanding any other provision of law, no person shall be subject to any penalty for failing to comply with a collection of information if it does not display a currently valid OMB control number.</p> <p>PLEASE DO NOT RETURN YOUR FORM TO THE ABOVE ADDRESS.</p>					
1. REPORT DATE (DD-MM-YYYY) 01-05-2009		2. REPORT TYPE Contractor Report		3. DATES COVERED (From - To)	
4. TITLE AND SUBTITLE A Mode-Shape-Based Fault Detection Methodology for Cantilever Beams			5a. CONTRACT NUMBER NNH06CC03B		
			5b. GRANT NUMBER		
			5c. PROGRAM ELEMENT NUMBER		
6. AUTHOR(S) Tejada, Arturo			5d. PROJECT NUMBER		
			5e. TASK NUMBER		
			5f. WORK UNIT NUMBER 645846.02.07.07.07		
7. PERFORMING ORGANIZATION NAME(S) AND ADDRESS(ES) NASA Langley Research Center Hampton, VA 23681-2199			8. PERFORMING ORGANIZATION REPORT NUMBER		
9. SPONSORING/MONITORING AGENCY NAME(S) AND ADDRESS(ES) National Aeronautics and Space Administration Washington, DC 20546-0001			10. SPONSOR/MONITOR'S ACRONYM(S) NASA		
			11. SPONSOR/MONITOR'S REPORT NUMBER(S) NASA/CR-2009-215721		
12. DISTRIBUTION/AVAILABILITY STATEMENT Unclassified - Unlimited Subject Category 64 Availability: NASA CASI (443) 757-5802					
13. SUPPLEMENTARY NOTES NASA Postdoctoral Program Research Advisor: Benedetto L. Di Vito, Langley Research Center This work was performed while the author was at Langley Research Center under the NASA Postdoctoral Program administered under contract with Oak Ridge Associated Universities, Oak Ridge, Tennessee.					
14. ABSTRACT An important goal of NASA's Internal Vehicle Health Management program (IVHM) is to develop and verify methods and technologies for fault detection in critical airframe structures. A particularly promising new technology under development at NASA Langley Research Center is distributed Bragg fiber optic strain sensors. These sensors can be embedded in, for instance, aircraft wings to continuously monitor surface strain during flight. Strain information can then be used in conjunction with well-known vibrational techniques to detect faults due to changes in the wing's physical parameters or to the presence of incipient cracks. To verify the benefits of this technology, the Formal Methods Group at NASA LaRC has proposed the use of formal verification tools such as PVS. The verification process, however, requires knowledge of the physics and mathematics of the vibrational techniques and a clear understanding of the particular fault detection methodology. This report presents a succinct review of the physical principles behind the modeling of vibrating structures such as cantilever beams (the natural model of a wing). It also reviews two different classes of fault detection techniques and proposes a particular detection method for cracks in wings, which is amenable to formal verification. A prototype implementation of these methods using Matlab® scripts is also described and is related to the fundamental theoretical concepts.					
15. SUBJECT TERMS Structural health monitoring; Fault detection; Fiber optic sensors; Strain measurement; Cantilever beams					
16. SECURITY CLASSIFICATION OF:			17. LIMITATION OF ABSTRACT	18. NUMBER OF PAGES	19a. NAME OF RESPONSIBLE PERSON
a. REPORT	b. ABSTRACT	c. THIS PAGE			STI Help Desk (email: help@sti.nasa.gov)
U	U	U	UU	42	19b. TELEPHONE NUMBER (Include area code) (443) 757-5802

